ARCHIVIO ISTITUZIONALE
DELLA RICERCA

Alma Mater Studiorum Università di Bologna
Archivio istituzionale della ricerca

Geometric optimization of a lid-driven cavity with two rectangular intrusions under mixed convection heat transfer: A numerical investigation motivated by constructal design

This is the final peer-reviewed author's accepted manuscript (postprint) of the following publication:

Published Version:
Rodrigues, P.M., Biserni, C., de Escobar, C.C., Rocha, L.A.O., Isoldi, L.A., dos Santos, E.D. (2020). Geometric optimization of a lid-driven cavity with two rectangular intrusions under mixed convection heat transfer: A numerical investigation motivated by constructal design. INTERNATIONAL COMMUNICATIONS IN HEAT AND MASS TRANSFER, 117, 1-14 [10.1016/j.icheatmasstransfer.2020.104759].

Availability:
This version is available at: https://hdl.handle.net/11585/767363 since: 2020-07-29

Published:

DOI: http://doi.org/10.1016/j.icheatmasstransfer.2020.104759

Terms of use:

Some rights reserved. The terms and conditions for the reuse of this version of the manuscript are specified in the publishing policy. For all terms of use and more information see the publisher's website.

This item was downloaded from IRIS Università di Bologna (https://cris.unibo.it/).
When citing, please refer to the published version.

(Article begins on next page)

18 December 2024

GEOMETRIC OPTIMIZATION OF A LID-DRIVEN CAVITY WITH TWO RECTANGULAR INTRUSIONS UNDER MIXED CONVECTION HEAT TRANSFER: A NUMERICAL INVESTIGATION MOTIVATED BY CONSTRUCTAL DESIGN

P.M.Rodrigues[1], C. Biserni[2,*], C.C. de Escobar[1], L.A.O. Rocha[3], L.A. Isoldi[1], E.D. dos Santos[1]

[1] Graduate Program in Computational Modeling, Federal University of Rio Grande – FURG, Italia Av., km 8, 96203-900, Rio Grande, RS, Brazil

[2] Department of Industrial Engineering, Alma Mater Studiorum, University of Bologna, Viale Risorgimento 2, 40136 Bologna, Italy.

[3] Mechanical Engineering Graduate Program, University of Vale do Rio dos Sinos – UNISINOS, São Leopoldo, 93.022-750, RS, Brazil

* Corresponding author: cesare.biserni@unibo.it

ABSTRACT

The present work aims at the geometric optimization, by means of constructal design and exhaustive search, of two rectangular fins inserted in a lid-driven cavity subjected to unsteady, incompressible, laminar, two-dimensional mixed convective flow with stable stratification. The main purpose is to maximize the dimensionless heat transfer rate ($\tilde{q}'$) and time and spatial-averaged Nusselt number ($\overline{Nu}_H$). The domain presents three constraints: cross-sectional areas for each fin and total area of the cavity. Two degrees of freedom are investigated, height/length ratios of the left and right rectangular fin (H_1/L_1 and H_2/L_2), considering three different fraction areas for fins and two different Richardson numbers Ri = 0.1 and 1.0, representing two conditions for mixed convective flow. All cases have constant Reynolds and Prandtl numbers (Re_H = 400 and Pr = 6.0). The conservation equations of mass, momentum, and energy are solved using the Finite Volume Method. Recommendations for fins shapes were strongly affected by the performance indicators chosen. Results also indicated that asymmetric configurations for the fins with different fraction areas for each fin led to the best thermal performance. Moreover, the optimal shapes and the effect of degrees of freedom over performance indicators were also affected by the Richardson numbers investigated.

Keywords: Constructal Design, Mixed Convection, Lid-driven Flows, Cavity, Rectangular Fins.

Nomenclature

A	Area of the cavity [m²]
A_1	Area of the left fin [m^2]
A_2	Area of the right fin [m^2]
C_p	Specific heat [J kg^{-1} K^{-1}]
g	Gravity acceleration in y-direction [m s^{-2}]
Gr_H	Grashof number based on cavity height [-]
H	Cavity height [m]
H_1	Height of the left fin [m]
H_2	Height of the right fin [m]
k	Thermal conductivity of the fluid [W m^{-1} K^{-1}]
L	Length of the cavity [m]
L_1	Length of the left fin [m]
L_2	Length of the right fin [m]
n^*	Normal dimensionless coordinate to the fin surfaces
Nu_H	Nusselt number based on cavity height [-]
$\overline{Nu_H}$	Spatial-averaged Nusselt number based on cavity height [-]
$\overline{Nu_{H,m}}$	Once maximized Nusselt number based on cavity height [-]
$\overline{Nu_{H,mm}}$	Twice maximized Nusselt number based on cavity height [-]
P	Pressure [N m^{-2}]
Pr	Prandtl number [-]
$\bar{q}$	Heat transfer rate between the cavity flow and fins [W]
q'	Heat transfer rate per unit length [W m^{-1}]
$\tilde{q}'$	Dimensionless heat transfer rate [-]
$\tilde{q}'_{\mathrm{m}}$	Once maximized dimensionless heat transfer rate [-]
$\tilde{q}'_{mm}$	Twice maximized dimensionless heat transfer rate [-]
Ra_H	Rayleight number based on cavity height [-]
Re_H	Reynolds number based on cavity height [-]

Ri	Richardson number [-]
T	Temperature [K]
T_∞	Free-stream temperature [K]
u	Velocity in the x-direction [m s^{-1}]
v	Velocity in the y-direction [m s^{-1}]
W	Depth of the cavity in z-direction [m]
x	Spatial coordinate in x-direction [m]
y	Spatial coordinate in y-direction [m]
z	Spatial coordinate in z-direction [m]

Greek Symbols

α	Thermal difusivity [m^2 s^{-1}]
β	Thermal expansion coefficient [K^{-1}]
ν	Kinematic velocity [m^2 s^{-1}]
μ	Fluid dynamic viscosity [kg m^{-1} s^{-1}]
ρ	Density [kg m^{-3}]
ϕ_T	Total fraction between fins and cavity areas [-]
ϕ_1	Fraction area of the left fin [-]
ϕ_2	Fraction area of the right fin [-]

Subscript

m	Once maximized
mm	Twice maximized
o	Once optimized
oo	Twice optimized

Superscript

*	Dimensionless variables
_	Spatial-averaged variables

1. INTRODUCTION

Several engineering problems can be idealized by cavity flows with convective heat transfer, such as solar air heater, electronic packaging, and spacing between adjacent fins in heat exchangers. The mixed convection mechanism in lid-driven cavities occurs

due to two simultaneous and complex flow generation processes. One process is caused by the shear flow produced by the lid-driven wall's movement, while the other is due to buoyancy flow generated by non-homogeneity of the cavity thermal boundaries. Understanding these mechanisms is of great importance from technical and engineering perspectives.

In this context, flow inside cavities has been broadly studied over the years [1-6]. Concerning convection heat transfer, several studies have been done to achieve a better understanding of the fluid dynamic and thermal behavior of forced convection [4, 5] and mixed convection [7, 8] in lid-driven cavity flows. Various contributions about "ordinary" lid-driven cavity flows, i.e., without inserted fins, have been pointed out. For illustration, the influence of different cross-sectional shapes for the cavity, e.g., rectangular, semi-circular, and trapezoidal over fluid and thermal behavior, has been investigated [6, 9-11]. Recently, new contributions have been produced about convection heat transfer considering nanofluid and porous medium in the enclosure domain [5, 12].

In addition, relevant studies concerning obstacles or fins inside a lid-driven cavity have been explored in literature. For instance, Oztop et al. [13] examined a lid-driven airflow under mixed convection within a square enclosure having an intruded circular body. Results showed that the thermal conductivity becomes insignificant in the thermal behavior for small values of the diameter of the body. Afterward, Khanafer and Aithal [14] investigated numerically a lid-driven cavity with a rotating cylinder, varying two essential parameters, i.e. the Richardson number and the non-dimensional angular velocity of the cylinder. It was shown that time and spatial averaged Nusselt number increased with the augmentation in the clockwise angular velocity of the cylinder for various Richardson numbers. The problem of heat transfer by mixed convection in a cavity considering a heat-conducting solid in a backward step form was investigated by Gibanov et al. [15]. More recently, Gangaware et al. [16] examined the mixed convection flow in a lid-driven cavity with intruded heated triangular block. The body was subjected to constant heat flux and its position was varied along the vertical centerline of the cavity. In addition, it is worth mentioning Refs. [17-19], which fall in the same domain.

Constructal Law is a physical principle postulating that for any finite flow system to persist in time (to survive), its design must evolve in such a way to easily the internal streams that flow through the thermodynamic system [20-22]. Constructal Design is the method based on objectives (performance indicators) and constraints used to apply the physical principle (Constructal Law) to investigate designs and rhythms along the time

of animate or inanimate flow systems [23]. Constructal Design proved to be fully versatile and interdisciplinary, since it has been adopted in the context of designs of natural flow, such formation of trees and river basin [22], economy and technology [23], global circulation, and climate [24], human movement urban traffic and social dynamics [25]. Regarding the original focus of Constructal Design, several geometric investigations in the engineering field have been performed, including turbines, renewable energy [26], solid mechanics ("flow of stresses"), refrigeration and heat exchangers [27-34].

Recently, some works have involved both Constructal Design and Exhaustive Search for the geometrical optimization of fins intruded in lid-driven convective cavity flows. On this regard, Dos Santos et al. [35] employed the Constructal Design method to evaluate the effect of a single rectangular fin inserted in the lower surface of forced convective lid-driven square cavity flow, considering various Reynolds numbers ($10.0 \leq Re_H \leq 10^3$) and one magnitude of Prandtl number ($Pr = 0.71$). Results showed a strong influence of the fin geometry over the heat transfer between one rectangular fin and the surrounding flow, measured by the spatial and time-averaged Nusselt number in the fin surfaces. Moreover, optimal shapes had a strong dependence on the Reynolds number. Similarly, the same geometric configuration was investigated by Lorenzini et al. [36] for different Reynolds and Rayleigh numbers. It has been demonstrated that fin geometry had substantial influence over the Nusselt number in the fin. Furthermore, different magnitudes of Rayleigh number influenced the effect of the height/length ratio of the fin over the Nusselt number, especially for lower magnitudes of Reynolds number ($Re_H = 10$). Aldrighi et al. in Ref. [37] studied a laminar, steady, and forced convective lid-driven square cavity flow with rectangular fin inserted in the center of different cavity surfaces. It was shown that the highest Nu_H was obtained for fins intruded in the downstream surface for $50 \leq Re_H \leq 500$. More recently, Razera et al. [38] examined a semi-elliptical fin inserted in a lid-driven square cavity with mixed convection. The evaluation of Nusselt number was carried out for different Reynolds ($10.0 \leq Re_H \leq 10^3$) and Rayleigh ($10^3 \leq Ra_H \leq 10^6$) numbers, showing that the optimal configuration presented a gain of around 40% in the thermal performance compared to other geometries.

In this context, the present work is aimed at the geometric optimization of a lid-driven cavity under mixed convective, incompressible, laminar flows in a two-dimensional domain. The performance indicators are the Nusselt number ($\overline{Nu_H}$) and the dimensionless heat transfer rate ($\tilde{q}'$). The cavity has two rectangular intrusions into the

lower surface. The geometry of the two fins is varied using the Constructal Design method and optimized using an exhaustive search, to obtain the best shapes, leading to the highest thermal performance. The sensitivity of the degrees of freedom of the domain has also been tested. All simulations have been performed for a stable stratified mixed convection flow with Re_H = 400, Pr = 6.0 and considering two different Richardson numbers (Ri = Gr_H/Re_H^2 = 0.1 and 1.0), which represent respectively a flow dominated by forced convective forces and an equilibrated condition between forced and natural convection, in coherence with Ref. [1]. Finally, the effect of different fraction areas for each of the two studied fins has been contemplated.

2. MATHEMATICAL MODELING

The geometric domain is considered two-dimensional and the flow is laminar, transient, and incompressible. In spite of transient simulations, results for heat transfer rate and Nusselt number are computed when the flow reaches the steady state. The thermophysical properties of the flow are kept constant throughout the domain, except for density, which is taken into account with the use of Boussinesq approximation [39]. The differential equations that describe the conservation equations of mass, momentum, and energy for a two-dimensional lid-driven cavity flow with the above considerations are given by Bejan in Ref. [40]:

$$\frac{\partial u}{\partial x}+\frac{\partial v}{\partial y}=0 \tag{1}$$

$$\frac{\partial u}{\partial t}+u\frac{\partial u}{\partial x}+v\frac{\partial u}{\partial y}=-\frac{1}{\rho_0}\frac{\partial p}{\partial x}+\upsilon\left(\frac{\partial^2 u}{\partial x^2}+\frac{\partial^2 u}{\partial y^2}\right) \tag{2}$$

$$\frac{\partial v}{\partial t}+u\frac{\partial v}{\partial x}+v\frac{\partial v}{\partial y}=-\frac{1}{\rho_0}\frac{\partial p}{\partial y}+\upsilon\left(\frac{\partial^2 v}{\partial x^2}+\frac{\partial^2 v}{\partial y^2}\right)+g\beta\left(T-T_0\right) \tag{3}$$

$$\frac{\partial T}{\partial t}+u\frac{\partial T}{\partial x}+v\frac{\partial T}{\partial y}=\alpha\left(\frac{\partial^2 T}{\partial x^2}+\frac{\partial^2 T}{\partial y^2}\right) \tag{4}$$

where u and v are the velocities in x- and y- directions, ρ_0 is the fluid density at reference temperature, β is the thermal expansion coefficient, P is the pressure, υ is the kinematic viscosity of the fluid, α is the thermal diffusivity, T is the temperature, T_0 is the reference temperature, and g is the gravity in the y-direction.

2.1. Problem Formulation and Geometric Optimization Procedure

The analysis considers two-dimensional cavities with a square cross-section and two rectangular mounted fins, as depicted in Fig. 1. More precisely, the studied cavity has two fins inserted in the lower surface subjected to laminar and mixed convective flow. The velocity of the infinity plate placed in the superior surface of the cavity is obviously taken as reference for the computation of the Reynolds number ($Re_H = u_{max}H/\upsilon = 400$). It is also considered a stable stratification convective flow, i.e., the prescription of the highest temperature is performed on the upper surface. Regarding the thermal field, the upper surface of the cavity (infinite plate) is at a dimensionless temperature $T_s^* = 1$, while the two fins are at a lower temperature, $T_i^* = 0$. The lateral and inferior surfaces of the cavity are thermally insulated. As for fluid dynamic fields, it is imposed non-slip, and impermeability condition, i.e., dimensionless velocities are prescribed as null ($u^* = v^* = 0$). The influence of the buoyancy forces is accounted with the use of two different Grashof numbers ($Gr_H = 1.6 \times 10^5$ and 1.6×10^6), which led to two different Richardson numbers ($Ri = Re_H/Gr_H^2 = 0.1$ and 1.0). For all cases, a fixed Prandtl number is taken into account, precisely $Pr = 6.0$.

FIGURE 1

To generalize the results, all the parameters are presented in dimensionless form, as given below:

$$x^*, y^*, H^*, L^*, H_1^*, L_1^*, H_2^*, L_2^* = \frac{x, y, H, L, H_1, L_1, H_2, L_2}{A^{1/2}} \tag{5}$$

$$u^*, v^* = \frac{u, v}{u_{\max}} \tag{6}$$

$$T^* = \frac{T - T_{\min}}{T_{\max} - T_{\min}} \tag{7}$$

where H is the cavity height, L is the cavity length, H_1 is the left fin height, L_1 is the left fin length, H_2 is the right fin height, L_2 is the right fin length, A is the cavity area, u_{max} is the highest velocity imposed in the lid-driven surface, T_{min} is the lowest magnitude

temperature in the cavity flow imposed in the fins, and T_{max} is the highest magnitude temperature in the cavity flow imposed in the lid-driven surface.

The geometrical assessment is based on the definition of three restrictions, specifically the total area of the cavity and two fins areas (A, A_1, and A_2) which are given, respectively, by:

$$A = HL \tag{8}$$

$$A_1 = H_1 L_1 \tag{9}$$

$$A_2 = H_2 L_2 \tag{10}$$

The fins areas can be represented by the fraction between fins and cavity areas as:

$$\phi_1 = \frac{A_1}{A} \tag{11}$$

$$\phi_2 = \frac{A_2}{A} \tag{12}$$

The total fraction between fin and cavity areas, ϕ_T, is defined as:

$$\phi_T = \phi_1 + \phi_2 \tag{13}$$

In the present study, the fraction area of each fin, ϕ_1 and ϕ_2, is varied concomitantly with the other one, while the total fin fraction area is maintained constant at $\phi_T = 0.1$ for all simulations. More precisely, three scenarios have been taken into account: $\phi_1 = 0.03$ and $\phi_2 = 0.07$ (case 1), $\phi_1 = 0.05$ and $\phi_2 = 0.05$ (case 2) and $\phi_1 = 0.07$ and $\phi_2 = 0.03$ (case 3).

The problem has three degrees of freedom (DOF): H/L (ratio between height and length of the cavity), H_1/L_1 and H_2/L_2 (ratio between the height and length of the fins). The main purpose is to determine the ratios H_1/L_1 and H_2/L_2 that maximizes the heat transfer between the fins and surrounding flow, more precisely the dimensionless heat transfer rate per unit length ($\tilde{q}'$). The time and spatial averaged Nusselt number ($\overline{Nu_H}$) have also been computed as a performance indicator in previous works of fins intruded in lid-driven cavity convective flows. Then, it is also computed here for comparison with

$\tilde{q}'$. Moreover, the $\overline{Nu_H}$ associated with fins heat exchange area are used for computation of $\tilde{q}'$. The local Nu_H is given by:

$$Nu_H = \frac{\partial T^*}{\partial n^*} \tag{14}$$

where n^* represents a normal dimensionless coordinate to the fin surfaces.

For the sake of comparison between different shapes, it is computed the time and spatial-averaged Nusselt number for each fin. The spatial-averaged magnitude of Nu_H is defined by:

$$\overline{Nu_H} = \frac{1}{L_P}\int_{L_P} Nu_H dl \tag{15}$$

where L_p is the surface perimeter of each fin, and dl is the line of integration along the fin perimeter. After the computation of the spatial-averaged Nusselt number in each fin, the averaged value is adopted for geometrical evaluation of the problem. Considering that the heat exchange area can vary for different ratios of H_1/L_1 and H_2/L_2, it is also important to take into account the heat transfer rate. The heat exchange between the fins and the surrounding flow is obtained from a balance between the convective heat transfer coefficient (which depends on $\overline{Nu_H}$) and the fins' heat exchange areas. Therefore, it is also computed the heat transfer rate per unit length between the fins and the surrounding flow, as given by:

$$q' = \frac{\bar{q}}{W} = \bar{h} L_p \left(T_\infty - T_S\right) \tag{16}$$

where $\bar{h}$ is the spatial averaged convection heat transfer coefficient, $\bar{q}$ is the spatial averaged heat transfer rate, W is the cavity depth (cavity dimension in the normal plane of Fig. 1, i.e., in the z-axis direction) and T_∞ is the free-stream temperature.

Moreover, the time and spatial averaged dimensionless heat transfer rate per unit length can be written by:

$$\tilde{q}' = \frac{q'}{k\left(T_\infty - T_S\right)} = \overline{Nu_H}\tilde{L}_P \tag{17}$$

where k is the thermal conductivity of the fluid.

The spatial averaged parameters are calculated after the fluid flow reached the steady state for the computation of time-averaged magnitudes of Nusselt number and dimensionless heat transfer rate per unit length. For the present investigation, this condition is achieved when $t^* = t.u_{max}/H \geq 50$. Afterwards, the spatial averaged magnitudes of $\overline{Nu_H}$ and $\tilde{q}$ are obtained at each time step in the time interval of $50 \leq t^* \leq 100$, and a mean between the obtained magnitudes is performed for the prediction of time-averaged parameters.

The search for better configurations is conducted by using a combination of Constructal Design and exhaustive search, i.e., examining all the possible configurations. As recently discussed in the literature [26, 38], to complete the procedure of optimization, one must choose an optimization method to find the best performance and evaluate the effect of geometry over flow system performance. The performance indicators are the maximization of Nusselt number ($\overline{Nu_H}$) and dimensionless heat transfer rate per unit length ($\tilde{q}'$), Eqs. (14) – (16), and the geometric investigation is subjected to the problem constraints, Eqs. (11) – (13).

For sake of clarity, Figure 2 shows a flowchart of the numerical investigation. It is worth mentioning that ϕ_T is constant being equal to $\phi_T = 0.1$, and ϕ_1 and ϕ_2 are varied respecting Eq. (13), with the purpose to maximize $\tilde{q}'$ and $\overline{Nu_H}$. The optimization process is carried out in two phases. In the first step, the fin geometry is optimized by varying the ratio H_1/L_1, keeping fixed the ratio H_2/L_2 and both ϕ_1 and ϕ_2. Thus, the dimensionless heat transfer rate per unit length and time and spatial-averaged Nusselt number once maximized ($\tilde{q}'_{\mathrm{m}}$ and $\overline{Nu_{H,m}}$) are defined, and the corresponding optimal ratio H_1/L_1 is named the "once optimized ratio" $(H_1/L_1)_{\mathrm{o}}$. It is worth mentioning that the optimal ratio which maximizes $\tilde{q}'$ can be different from the optimal ratio that maximizes $\overline{Nu_H}$. In the second step, the same process carried out in step 1 is repeated for other values of the ratio H_2/L_2. The highest magnitudes of dimensionless heat transfer rate per unit length and Nusselt number are now the "twice maximized" $\tilde{q}'$ and $\overline{Nu_H}$, i.e., in analogy with the

notations introduced in step 1, $\tilde{q}'_{mm}$ and $\overline{Nu_{H,mm}}$. The corresponding optimal shapes are the twice optimized ratio of H_1/L_1, $(H_1/L_1)_{oo}$, and the once optimized ratio of H_2/L_2, $(H_2/L_2)_o$. For all investigations, the ratios H_1/L_1 and H_2/L_2 are analyzed in the range $0.3 \leq H_1/L_1, H_2/L_2 \leq 10.0$. The superior limit for the ratios $H_1/L_1 = H_2/L_2 = 10.0$ was established to avoid extremely thin configurations for the fins and intersection between the fins and superior cavity surface, being a sort of restriction for the present problem. The two optimization steps are performed for the above-mentioned three different magnitudes of ϕ_1 and ϕ_2: Case 1) $\phi_1 = 0.03$ and $\phi_2 = 0.07$, Case 2) $\phi_1 = 0.05$ and $\phi_2 = 0.05$ and Case 3) $\phi_1 = 0.07$ and $\phi_2 = 0.03$. Moreover, all geometric evaluations are performed for two different magnitudes of the Richardson number (Ri = 0.1 and 1.0), leading to a total amount of 486 simulated cases to examine all possible configurations here investigated.

FIGURE 2

3. NUMERICAL MODELING

For the numerical simulations, all geometries and meshes were constructed with the open-source program Gmsh 2.16.0 [41], in which the domain is discretized using finite rectangular volumes. The commercial CFD package FLUENT 14.0 [42], based on the Finite Volume Method [43, 44], is used to solve Eqs. (1)-(4) for different fin configurations (H_1/L_1 and H_2/L_2). The solver is pressure-based, and the velocity–pressure coupling is performed with the semi-implicit method for pressure-linked equation consistent SIMPLEC (Semi-Implicit Method for Pressure-Linked Equations Consistent) algorithm. For the solution of advective terms of conservation equations of momentum and energy, it is employed in the first-order upwind interpolation scheme. Moreover, the calculations are considered converged when the residuals for the mass, momentum, and energy between two consecutive iterations are less than 10^{-6}, 10^{-6} and 10^{-8}, respectively.

The grid independence is achieved when the relative deviation between the spatial-averaged Nusselt numbers obtained with two successive grids is less than 1.0 %. Thus, the relative deviation (RD) is given by:

$$RD(\%) = \left| \frac{\overline{Nu_H^i} - \overline{Nu_H^{i+1}}}{\overline{Nu_H^i}} \right| \times 100 \qquad (18)$$

where H is the height of the cavity, the superscript "i" represents the coarse mesh and "i+1' the refined mesh. After the realization of the tests, Table 1 shows that the mesh with 40,401 volumes is considered adequate for the proposed study, presenting a deviation that complies with the defined criterion.

Table 1. Analysis of mesh quality for Re_H = 400, Pr = 6.0, Ri = 0.1, $\phi_1 = 0.05$, $\phi_2 = 0.05$, $H_1/L_1 = 5.0$, $H_2/L_2 = 5.0$.

Number of volumes	$\overline{Nu_H}$	RD (%)
2,601	1.9922	8.6604
10,201	2.1648	2.3781
22,801	2.2162	1.000
40,401	2.2384	0.1064
63,001	2.2408	

To verify the present numerical methodology, transient velocity and temperature fields were generated for a classic case of the lid-driven square cavity without fins. It is considered an unsteady mixed convective flow with Re_H = 400 and Pr = 6.0. Results obtained with the present method are compared with those previously found in Dos Santos et al. [1] and Ji et al. [45]. In this problem, the fluid motion is caused by the imposition of velocity in the upper surface, while on the other surfaces, the velocity is null. In the thermal field, the heat transfer is due to the temperature difference between the upper and lower surfaces of the cavity, while the lateral surfaces are thermally insulated. As the boundary condition, the highest temperature (T^* = 1.0) is imposed on the upper surface while the lowest temperature is maintained on the lower surface (T^* = 0.0). More precisely, the instantaneous fields of velocity and temperature are computed in three monitoring points: P1 (X^* = 0.5, Y^* = 0.27), P2 (X^* = 0.5, Y^* = 0.48) and P3 (X^* = 0.5, Y^* = 0.93) which are the same coordinates supervised in the work of Ji et al. [45]. The velocity and temperature profiles for three monitor points for a flow with Re_H = 400 and Pr = 6.0 obtained here and those predicted by Dos Santos et al. [1] and Ji et al. [45] are presented in Figs. 3(a) – (f). Results showed that the instantaneous velocity and temperature fields predicted in the three monitoring points have similar behavior to that previously predicted in the literature. A slight deviation for the thermal field is noticed for the superior region of the cavity (X^* = 0.5, Y^* = 0.93) in the range of time $8 \leq t^* \leq 18$ in comparison with the results presented by Ji et al. [45]. In spite of this, results present a

strong agreement with the previous fields predicted in literature, so that the code can be considered verified and calibrated.

FIGURE 3

4. RESULTS AND DISCUSSION

4.1. Geometric Investigation for Re_H = 400, Pr = 6.0 and Ri = 0.1

Two performance indicators have been here taken into account in the geometric optimization procedure, precisely the dimensionless heat transfer rate per unit length ($\tilde{q}'$) and time and spatial-averaged Nusselt number ($\overline{Nu_H}$), for Ri = 0.1. Results of geometric investigation for three different scenarios are presented in the following order: case 1 (ϕ_1 = 0.03 and ϕ_2= 0.07), case 2 (ϕ_1 = 0.05 and ϕ_2= 0.05) and case 3 (ϕ_1 = 0.07 and ϕ_2= 0.03).

More specifically, the first level of investigation, i.e. Ri = 0.1 and case 1 (ϕ_1 = 0.03 and ϕ_2= 0.07) is shown in Fig. 4, where the dimensionless heat transfer rate per unit length ($\tilde{q}'$) is presented versus the ratio H_1/L_1, Fig. 4a, and spatial-averaged Nusselt number, ($\overline{Nu_H}$), is highlighted with the variation of the same parameter H_1/L_1, Fig. 4b. As a general trend, Fig. 4a illustrates that the increase of H_1/L_1 leads to an augmentation of $\tilde{q}'$ for all ratios H_2/L_2 investigated. Moreover, higher values of heat transfer rate are achieved as H_2/L_2 increases. Thus, the ratio H_2/L_2 = 10.0 conducts to the best performance considering $\tilde{q}'$ as performance indicator. These results are coherent with the augmentation of the heat exchange area of the fins as H_1/L_1 and H_2/L_2 increase. Nonetheless, the right fin has a higher portion of area (ϕ_2), thus affecting to more extent the values of $\tilde{q}'$. In brief, among the analyzed geometries, it is possible to observe that the best performance is achieved for the highest intrusion of the fins, i.e., when $(H_2/L_2)_o$ = 10.0 and $(H_1/L_1)_{oo}$ = 10.0. The best configuration led to a magnitude of $\tilde{q}'$ nearly 120% higher than the worst one (H_2/L_2 = 0.9, H_1/L_1 = 0.3). Contrarily, Figure 4b shows that intermediate values of the ratio H_1/L_1 are associated to the highest magnitude of $\overline{Nu_H}$. In addition, a general trend of decrease of $\overline{Nu_H}$ is observed when $H_1/L_1 \geq 3.0$, for different magnitudes of H_2/L_2 investigated. However, a remarkable exception emerges with

reference to the case H_2/L_2 = 3.0, where an augmentation of $\overline{Nu_H}$ magnitude is noticed for $H_1/L_1 \geq 6.0$. Moreover, for H_2/L_2 = 5.0, it can be noticed that $\overline{Nu_H}$ has the highest magnitude for the lowest ratio of H_1/L_1, the only case in which this behavior was observed. Concerning the effect of H_1/L_1 over $\overline{Nu_H}$ for different values of H_2/L_2, there is a tendency that lower H_2/L_2 ratios lead to higher values of $\overline{Nu_H}$. For lower ratios of H_2/L_2, the main vortex is not suppressed in the right and upper portion of the cavity. Finally, among the curves shown in Fig 4b, the best configuration is obtained for $(H_2/L_2)_o$ = 0.3 and $(H_1/L_1)_{oo}$ = 1.0: the performance proves to be 49% superior to the $\overline{Nu_H}$ obtained for the worst case, i.e. H_2/L_2 = 7.0 and H_1/L_1 = 10.0.

In general, the results of Fig. 4 demonstrate that the effect of the variation of H_1/L_1 over $\tilde{q}'$ and $\overline{Nu_H}$, and consequently the optimal geometric configuration are strongly affected by the choice of performance indicator, which has always been an important focus in constructal design. Here, the heat transfer rate between the cavity flow and the fins is obtained from a balance between the convective heat transfer coefficient (which directly depends on Nusselt number) and the heat exchange area. Then, another important observation is that, under the present thermal and geometric conditions, the augmentation of the heat transfer area compensates for the decrease of Nusselt number caused by the restriction of fluid flow in the cavity, for the cases where the fins are highly intruded in the cavity.

FIGURE 4

Temperature fields with the best and worst performances for different ratios of H_2/L_2 are presented in Fig. 5 and provide a better understanding of the geometry influence for Ri = 0.1 and case 1. Regarding the analysis of $\tilde{q}'$, the ratios chosen are H_2/L_2 = 0.9 and 10.0, whereas for analyses of $\overline{Nu_H}$ the ratios H_2/L_2 = 0.3 and 7.0 are presented. For each of these ratios, two different values of H_1/L_1 were chosen, based on the criterion of the best and worst performance with reference to each performance indicator ($\tilde{q}'$ and $\overline{Nu_H}$).

More specifically, Figures 5a and 5b show in sequence the thermal fields for H_1/L_1 = 0.3 and $(H_1/L_1)_o$ = 10.0 with H_2/L_2 = 0.9, considering $\tilde{q}'$ as a performance indicator. Based on pure observation, the intrusion of the left fin led to a higher interaction with the main vortex, conducting to an augmentation of heat transfer rate. The heat transfer once maximized for the ratio $(H_1/L_1)_o$ = 10.0, Fig. 5b, is $\tilde{q}'_m$ = 5.4947, which represents a magnitude 57% higher than that reached for the ratio H_1/L_1 = 0.3 (Fig. 5a). Figures 5c and 5d highlight the thermal fields for H_1/L_1 = 0.3 and $(H_1/L_1)_o$ = 10.0 for H_2/L_2 = 10.0, considering the same performance indicator $\tilde{q}'$. The difference for these new configurations is the more pronounced insertion of the right fin into the cavity domain in comparison with the scenarios of Figs. 5a and 5b. This configuration caused an evolution of the main vortex toward the upstream surface of the cavity. Results also indicated that, in spite of hindering of the main vortex in the superior region of the cavity, the main vortex interacts with a more amount of area of the cooled fin, especially the right-side fin. In other words, even though the main vortex tends to be hindered, the configurations $(H_2/L_2)_o$ = 10.0 and $(H_1/L_1)_{oo}$ = 10.0 led to the twice maximized dimensionless heat transfer rate per unit length of $\tilde{q}'_{mm}$ = 7.6783 (Fig. 5d). It is worth mentioning that, once the fraction areas of the fins are different, the imposition of the same ratio ($H_1/L_1 = H_2/L_2$) led to an asymmetric configuration.

Figures 5e – 5h show the best and worst shapes using $\overline{Nu}_H$ as a performance indicator, for two magnitudes of H_2/L_2, $(H_2/L_2)_o$ = 0.3 (Figs. 5e – 5f) and H_2/L_2 = 7.0 (Figs. 5g – 5h). The thermal fields distribution demonstrates that low magnitudes of H_2/L_2 and H_1/L_1 led to the best performance due to the higher intensity of the main vortex. In spite of this, the variation of $\overline{Nu}_H$ for the cases with the lowest and highest magnitude is not significant, so that the heat exchange area defines practically the heat transfer rate. More specifically, the twice maximized Nusselt number, $\overline{Nu}_{H,mm}$, obtained for $(H_2/L_2)_o$ = 0.3 and $(H_1/L_1)_{oo}$ = 1.0 (Fig. 5e) is nearly 8% superior in comparison with the case with H_2/L_2 = 0.3 and H_1/L_1 = 10.0 (Fig. 5f). However, the heat exchange area of the case presented in Fig. 5f is almost 43% superior to that of Fig. 5e. In this sense, the dimensionless heat transfer rate obtained for the configuration of Fig. 5f is superior to that found for Fig. 5e.

FIGURE 5

The best shapes obtained in Figs. 4 and 5 are summarized in Fig. 6. More precisely, Fig. 6 shows the influence of the ratio H_2/L_2 over the $\tilde{q}'_m$ (Fig. 6a) and $\overline{Nu}_{H,m}$ (Fig. 6b) as well as their optimal geometries $(H_1/L_1)_o$ for scenario 1. In the case of $\tilde{q}'_m$ (Fig. 6a), it can be observed that the ratio $(H_1/L_1)_o$ = 10.0 is constant, which is a consequence of the best design obtained with the most intruded fin in the cavity. Fig. 6a also shows the influence of the ratio H_2/L_2 on the once maximized dimensionless heat transfer rate per unit length ($\tilde{q}'_m$). For lower ratios of H_2/L_2 ($H_2/L_2 \leq 6.0$), a slight variability of $\tilde{q}'_m$ is detected, which suggests that the right fin does not have a strong influence on the thermal exchange for this ratio interval. This behavior can be related to an equilibrium between the decrease of $\overline{Nu}_{H,m}$ (Fig. 6b) and the augmentation of the fin area for $H_2/L_2 \leq 6.0$. In the interval range of $6.0 \leq H_2/L_2 \leq 10.0$, the magnitude of $\overline{Nu}_{H,m}$ increases another time. This behavior associated with the augmentation of fin areas led to a significant increase of once maximized heat transfer rate ($\tilde{q}'_m$).

Another important observation captured in Fig. 6 is that the effect of H_2/L_2 over $\tilde{q}'_m$ and $\overline{Nu}_{H,m}$, as well as, the optimal ratios of $(H_1/L_1)_o$ is quite different. For the assessment of $\tilde{q}'_m$ the best shape is achieved when the fins have the highest intrusion in the cavity, while for $\overline{Nu}_{H,m}$ there are two optimal regions, the most prominent for the lowest magnitude of H_2/L_2 and a local point of optimum for the superior extreme of H_2/L_2 (H_2/L_2 = 10.0). Again, results showed that the balance between the Nusselt number and the heat exchange area is important for defining the design, which maximizes the heat transfer rate. Moreover, the effect of H_2/L_2 on the $(H_1/L_1)_o$ is constant for $\tilde{q}'_m$, and it has a sensible variation for $\overline{Nu}_{H,m}$.

FIGURE 6

Concerning the investigation of case 2 (ϕ_1 = 0.05 and ϕ_2= 0.05) for Ri = 0.1, Fig. 7 shows the effect of the variation of the ratio H_1/L_1 over the heat flux $\tilde{q}'$ (Fig. 7a) and spatial-averaged Nusselt number $\overline{Nu}_H$ (Fig. 7b). The curves depicted in Fig. 7a shows a similar trend of increase to that presented in Fig. 4a, i.e., the augmentation of H_1/L_1 leads

to an increase of $\tilde{q}'$ for all ratios H_2/L_2. Moreover, higher values of heat transfer rate are achieved for the uppermost magnitudes of H_2/L_2. In addition, for the majority interval ratio of H_1/L_1, the best geometry found is $H_2/L_2 = 10.0$. One exception is observed for the ratio $H_2/L_2 = 3.0$ in the interval of $3.0 \leq H_1/L_1 \leq 7.0$. In this sense, among all the analyzed geometries, the best ones are $(H_2/L_2)_o = 10.0$ and $(H_1/L_1)_{oo} = 10.0$. Fig. 7b shows the effect of the ratio H_1/L_1 on the $\overline{Nu}_H$ for case 2. Based on pure observation in Fig. 7(b), it can be noted that the ratios $H_2/L_2 = 0.3$ and 0.5 ore in correspondence to the highest $\overline{Nu}_H$ in the lowest magnitudes of H_1/L_1. As the ratio H_2/L_2 increases, the optimum ratio H_1/L_1 tends to be equal to 10.0, i.e., the other extreme. For this geometric evaluation, a variation of nearly 54% on $\overline{Nu}_H$ is achieved when comparing the best configuration ($(H_1/L_1)_{oo} = 0.3$ and $(H_2/L_2)_o = 0.3$)) with the worst case ($H_1/L_1 = 0.5$ and $H_2/L_2 = 10.0$).

The above remarks indicated that it is interesting to evaluate the effect of fin fractions ϕ_1 and ϕ_2 on the thermal response the for the cases 1 and 2. It is possible to notice that the effect of H_1/L_1 over $\tilde{q}'$ is similar for both scenarios 1 and 2. However, the magnitudes for different ratios of H_2/L_2 are more concentrated for case 2, while for case 1, the performance reached with $(H_2/L_2)_o = 10$ is significantly superior than that achieved for other ratios of H_2/L_2. As for the other performance indicator $\overline{Nu}_H$, the effect of H_1/L_1 over $\overline{Nu}_H$ is different for cases 1 and 2, especially for the highest magnitudes of H_1/L_1 where $\overline{Nu}_H$ present different trends (Figs. 4b and 7b).

FIGURE 7

The best shapes reached in Fig. 7 are summarized and presented in Fig. 8. More precisely, Fig. 8 shows the influence of the variation of the ratio H_2/L_2 over $\tilde{q}'_m$ and $\overline{Nu}_{H,m}$ as well as their optimal geometries $(H_1/L_1)_o$ for case 2. Regarding the performance indicator $\tilde{q}'_m$ (Fig. 8a), it can be seen that the ratio $(H_1/L_1)_o = 10.0$ is constant, which is matching to the result shown for case 1 (Fig. 6a). In addition, Fig. 8a shows a similar trend with more slight differences between the highest and lowest magnitudes of $\tilde{q}'_m$. Moreover, the fluctuation of $\tilde{q}'_m$ with H_2/L_2 is more intense with reference to case 2 than for case 1: this behavior can be observed in the range $0.5 \leq H_2/L_2 \leq 6.0$. In other words, changes in fraction areas from case 1 to case 2 determine the scales of $\tilde{q}'_m$, but do not

have significant impact on the effect of the ratio H_2/L_2 over $\tilde{q}'_m$ and $(H_1/L_1)_o$. In Fig. 8b, a decrease of $\overline{Nu}_{H,m}$ is observed as the ratio H_2/L_2 increases. More specifically, for $H_2/L_2 \geq 1.0$, the ratio $(H_1/L_1)_o = 10.0$ becomes the optimal one. In dissimilarity with Fig. 6b, results showed that passing from scenario 1 to scenario 2 influenced significantly the effect of the ratio H_2/L_2 over $\overline{Nu}_{H,m}$ and $(H_1/L_1)_o$. In general, it has been demonstrated that the variation of fin fraction area from case 1 to case 2 was more important for the investigation of the once maximized Nusselt number than for the once maximized heat transfer rate.

FIGURE 8

Figures 9a-c show the temperature fields for three points in the curve of Fig. 8a. It can be seen that the higher insertion of both fins leads to better results for $\tilde{q}'_m$, even though the main vortex becomes suppressed for higher ratios H_2/L_2 (Fig. 9c). In this sense, the twice maximized heat transfer rate is $\tilde{q}'_{mm} = 6.8345$ for the optimal ratios $(H_1/L_1)_{oo} = (H_2/L_2)_o = 10.0$. One possible explanation for this behavior is the augmentation of the contact area available as the fin insertion increases and the consequent spreading of the main vortex towards the upstream surface of the lid-driven cavity. Figures 9d-e confirm that increasing the ratio H_2/L_2, with higher insertion of the right fin on the cavity, tends to suppress the main vortex.

On the other hand, there is an augmentation of the vortex for lower ratios H_2/L_2 (Fig. 9d). In this sense, because the flow comes from left to right into the cavity, the right fin possesses more influence in decreasing $\overline{Nu}_{H,m}$, i.e., smoothing the thermal gradients between the fins and surrounding flow. Another interesting observation is concerned with the best geometry found for $\tilde{q}'_{mm}$, which is the worst in terms of $\overline{Nu}_{H,m}$. Then, results indicated that the decrease of $\overline{Nu}_{H,mm}$ from the optimal shape, $(H_1/L_1)_{oo} = (H_2/L_2)_o = 0.3$, to the worst shape, considering the $\overline{Nu_H}$ as a performance indicator, is not enough to suppress the heat transfer rate, which increases with the augmentation of heat exchange area.

FIGURE 9

Figures 10 show the effect of the variation of the ratio H_1/L_1 over $\tilde{q}'$ (Fig. 10a) and over $\overline{Nu}_H$ (Fig. 10b), for Ri = 0.1 with reference to case 3 (ϕ_1 = 0.07 and ϕ_2= 0.03). Figure 10a shows that an increase of H_1/L_1 leads to the augmentation of $\tilde{q}'$ for all ratios H_2/L_2, except for the ratios where $H_1/L_1 \leq 0.7$. Among all the geometries analyzed, the best ones are for $(H_2/L_2)_o$= 10.0 and $(H_1/L_1)_{oo}$ = 10.0. Comparing with cases 1 (Fig. 4) and 2 (Fig. 7), it can be seen similar patterns as a general trend. The difference here is that the increase of ϕ_1 results in higher magnitudes $\tilde{q}'$ for all ratios of H_2/L_2 analyzed. One possible explanation for this behavior can be related to the flow movement from the upper right region of the cavity towards the center of the domain. Once the right-side fin is close to the downstream upper corner of the cavity, it is strongly subjected to the influence of the main vortex flow. On the opposite, the left-side fin is lower affected by the main vortex, and the increase of the cross-sectional area of this fin is important for the augmentation of global heat transfer rate. Figure 10b indicates, in general, two points of maximum $\overline{Nu}_H$ in the lowest and highest extremes of the ratio H_1/L_1. The behavior obtained here is more similar to that one achieved for case 2 (Fig. 7b). However, the variation of $\overline{Nu}_H$ between the best and worst cases is more intensive, and the local point of maximum in the lower extreme ratio of H_1/L_1 is more prominent.

FIGURE 10

Figures 11 show the influence of the ratio H_2/L_2 on $\tilde{q}'_m$ and $\overline{Nu}_{H,m}$ and their optimal geometries $(H_1/L_1)_o$ for case 3. More specifically, Figure 11a indicates that the same effect of the ratio H_2/L_2 over $(H_1/L_1)_o$ previously obtained for cases 1 (Fig. 6) and 2 (Fig. 8) is also detected in case 3, i.e., $(H_1/L_1)_o$ = 10.0 for all magnitudes of H_2/L_2. However, the effect of H_2/L_2 over $\tilde{q}'_m$ has changed from previous cases 1 and 2 (Fig. 6a and Fig. 8a). As for scenario 3, it is noticed an intermediate point of the highest magnitude for $\tilde{q}'_m$ for the once optimized ratio $(H_2/L_2)_o$ = 5.0. Comparing the best shapes reached for cases 1, 2 and 3 (Figs. 6a, 8a and 11a), the best shape for the cases 1 and 2 are located at $(H_2/L_2)_o$ = 10.0 with $\tilde{q}'_{mm}$ = 7.6784 and $\tilde{q}'_{mm}$ = 6.8345, respectively, whereas for case 3 the point is located at $(H_2/L_2)_{oo}$ = 5.0 and $\tilde{q}'_{mm}$ = 7.8407. In other words, the effect of increasing ϕ_1 results in an augmentation of $\tilde{q}'_{mm}$ and in the variation of the best ratio of $(H_2/L_2)_o$.

Figure 11b shows the influence of the ratio H_2/L_2 on the $\overline{Nu}_{H,m}$ and their optimal geometries $(H_1/L_1)_o$ for case 3. A decrease of $\overline{Nu}_{H,m}$ is observed as the ratio H_2/L_2 increases. Concerning the once optimized ratio $(H_1/L_1)_o$, for the $H_2/L_2 \leq 1.0$, the best value of $(H_1/L_1)_o$ is equal to 0.3 and for values of $H_2/L_2 \geq 1.0$ the ratio $(H_1/L_1)_o$ increases monotonically up to the asymptotic value, which is the highest magnitude of $(H_1/L_1)_o$. Comparing the three cases (1, 2, and 3), it can be noticed that the effect of H_2/L_2 over $\overline{Nu}_{H,m}$ and $(H_1/L_1)_o$ has a significant change from the case 1 to cases 2 and 3 (Figs. 6b, 8b, and 11b). In spite of slight differences, cases 2 and 3 presented a similar behavior.

In general, once the flow does not have a symmetrical behavior, due to formation of the main vortex from the upper and downstream corner towards the cavity center, the consideration of different cross-sectional areas for the left and right fins influenced the effect of geometry over the thermal performance for both indicators established in the present work. This influence showed more intense for the ratio H_2/L_2 once the right fin is placed closer to the region of the main vortex generation.

FIGURE 11

4.2. Geometric Investigation for Re_H = 400, Pr = 6.0 and Ri = 1.0

In this section, a similar investigation performed for the flow with Re_H = 400, Pr = 6.0 and Ri = 0.1 is performed with the aim to evaluate the influence of more intensive buoyancy forces (fixing Ri = 1.0) over the design of the rectangular fins inserted in lid-driven mixed convective flow. For sake of conciseness, only the results of case 2 (ϕ_1= 0.05 and ϕ_2 = 0.05) are presented in this section.

Figures 12 show the effect of the variation of the ratio H_1/L_1 on the dimensionless heat transfer rate ($\tilde{q}'$) (Fig. 12a) and spatial-averaged Nusselt number ($\overline{Nu}_H$) (Fig. 12b) for Ri = 1.0 and scenario 2 (ϕ_1 = 0.05 and ϕ_2= 0.05). A comparison with Ri = 0.1 (Fig. 7) highlights that the effect of the variation of H_1/L_1 over $\tilde{q}'$ has a similar behavior for both the investigated values of the Richardson number, Ri = 0.1 and 1.0. The sole difference is related to the range of magnitudes for different ratios of H_2/L_2. Once the main vortex is more restricted in the upper region of the cavity, the highest magnitudes of H_2/L_2 (e.g., H_2/L_2 = 5.0, 7.0, and 10.0) have a prominent performance in comparison with those reached for $H_2/L_2 \leq 1.0$. This variation in the magnitude of $\tilde{q}'$ between the highest and

lowest values of H_2/L_2 is not perceived for the case with Ri = 0.1. Concerning the effect of H_1/L_1 over $\overline{Nu}_H$, results reveal important differences with the variation of Richardson number from Ri = 0.1 to 1.0. For example, the highest magnitudes of $\overline{Nu}_H$ are obtained for the lowest curves of H_2/L_2 for all range of H_1/L_1 investigated when Ri = 0.1 and the opposite situation is noticed when Ri = 1.0. In other words, the lowest magnitudes of H_2/L_2 are associated with weak performance of $\overline{Nu}_H$ in a wide range of the ratio H_1/L_1. Moreover, it is worth mentioning that the effect of the ratio H_1/L_1 over $\overline{Nu}_H$ is also influenced by the Richardson number for all curves of H_2/L_2 investigated.

FIGURE 12

The best **s**hapes reached in Fig. 12 are summarized in Fig. 13, where the influence of the ratio H_2/L_2 over $\tilde{q}'_m$ and $\overline{Nu}_{H,m}$ as well as their respective optimal ratios $(H_1/L_1)_o$ for case 2, are shown graphically. In Fig. 13a, it can be observed that the ratio $(H_1/L_1)_o$ is constant and equal to 12.0, as occurred for case 2 with Ri = 0.1 (Fig. 8a). The behavior of $\tilde{q}'_m$ a function of H_2/L_2 obtained for Ri = 1.0, and Ri = 0.1 is also similar. The main difference is concerned with the lack of a local point of maximum for intermediate ratios of H_2/L_2 for the case with Ri = 1.0. It is also noticed differences in the magnitude of $\tilde{q}'_m$ for different Richardson numbers. For the investigation of $\overline{Nu}_{H,m}$, Fig. 13b shows a constant optimal ratio $(H_1/L_1)_o$ = 10.0, the same obtained when the performance indicator is $\tilde{q}'_m$. This behavior can be explained by the few sensibilities of the ratio H_2/L_2 over the once maximized Nusselt number ($\overline{Nu}_{H,m}$). It is worth mentioning that the variation of Richardson from Ri = 0.1 to Ri = 1.0 led to a significant variation on the effect of H_2/L_2 over $\overline{Nu}_{H,m}$.

The illustration of temperature fields for the best and worst geometries for both $\tilde{q}'_m$ and $\overline{Nu}_{H,m}$ related to Fig. 13 are depicted in Fig. 14. Based on pure observation for all fields, there is a trend of flow suppression on the top region of the cavity. This behavior is due to the difficulty of overcoming the buoyancy forces as a consequence of higher Ri and by the imposition of stably stratified mixed convective flow. In this sense, to facilitate the heat exchange, and thus increase $\tilde{q}'_m$, the right fin must have the highest possible

intrusion in the cavity, as shown in Fig. 14b. For $\overline{Nu}_{H,m}$, lower magnitudes of H_2/L_2 allowed a higher growth of the main vortex toward the lower region of the cavity and led to a slight superior magnitude of $\overline{Nu}_H$. In spite of this, the stable stratification in this case leads to few magnitudes of $\overline{Nu}_H$ and few differences between the best (Fig. 14d) and worst shapes (Fig. 14c), nearly 8.0%.

FIGURE 13

FIGURE 14

4.3. Optimal Shapes Obtained for Different Richardson and Fraction Areas

This section illustrates the results of a comparison focused on the best shapes for each investigated fraction areas of the fins (cases 1, 2 and 3), for two different Richardson numbers studied, Ri = 0.1 and 1.0, for both $\tilde{q}'_{mm}$ and $\overline{Nu}_{H,mm}$, and the respective optimal ratios, $(H_2/L_2)_o$ and $(H_1/L_1)_{oo}$.

As can be seen in Fig. 15a, the value of $\tilde{q}'_{mm}$ follows the following order: case 3 > case 1 > case 2 for Ri = 0.1. Comparing the worst with the best case, it was observed an increase of approximately 15% for $\tilde{q}'_{mm}$. Results also indicated that the twice optimized ratio $(H_1/L_1)_{oo}$ is insensitive to the fin fraction (ϕ_1 or ϕ_2) when the $\tilde{q}'_{mm}$ is defined as a performance indicator. Moreover, when Ri = 0.1, results indicated that the highest possible penetration of left-side fin enhances the heat transfer rate maximization. Additionally, for ϕ_1 = 0.03 and 0.05, the highest performance is achieved for the highest possible magnitude of $(H_2/L_2)_o$ = 10.0, i.e., for the highest intrusion of the right-side fin in the cavity. For ϕ_1 = 0.07, this ratio collapses to $(H_2/L_2)_o$ = 5.0. Once the heat exchange area of right-side fin decreases for this case, one possibility to improve the heat transfer rate is to allow the higher incidence of the main vortex in the cavity domain and improving the fluid contact with the right side. This effect can be achieved by diminishing the restriction of the right fin in the upper portion of the cavity. From Fig. 15b, the value of $\overline{Nu}_{H,mm}$ follows the order case 3 > case 1 > case 2. For asymmetric cases (cases 1 and 3), results also showed that the higher ϕ_1 is associated with an increase of $\overline{Nu}_{H,mm}$, i.e., geometrically, when the left fin has a higher area. This behavior is not intuitively expected

since the fin with a higher incidence of the main vortex must have a lower fraction area for two investigated performance indicators. Concerning the optimal shapes for $\overline{Nu}_{H,mm}$, the best case is obtained for $\phi_1 = 0.07$, $(H_2/L_2)_o = 0.3$ and $(H_1/L_1)_{oo} = 1.0$, whereas for the worst case for $\phi_1 = 0.03$, $(H_2/L_2)_o = (H_1/L_1)_{oo} = 0.3$.

FIGURE 15

Fig. 16 shows the temperature fields related to Fig. 15. Based on pure observation, for fraction areas $\phi_1 = 0.03$ and 0.07, asymmetric fins dimensions led to the best performance, while for the case with $\phi_1 = \phi_2 = 0.05$, a symmetric pattern leads to the best thermal performance, independently of the established performance indicator ($\tilde{q}'$ or $\overline{Nu}_H$). Another important observation is that the symmetric fins impose a higher restriction on the main vortex, leading to lower performance in comparison with the asymmetric distribution of the fins. The temperature fields for the optimal shapes considering $\overline{Nu}_{H,mm}$ as performance indicators are depicted in Figs. 16 d – f. As a general trend, for varied fraction areas the best shapes are achieved for small ratios of $(H_1/L_1)_{oo}$ and $(H_2/L_2)_o$, contrarily to which is noticed for the cases where it is needed to maximize $\tilde{q}'_{mm}$. The best shapes also presented asymmetric patterns for the cases with $\phi_1 = 0.03$ and 0.07 and symmetric for the cases with $\phi_1 = \phi_2 = 0.05$. In spite of the highest magnitude of the Nusselt number for lower magnitudes of $(H_1/L_1)_{oo}$ and $(H_2/L_2)_o$, the heat exchanger area is not enough to compensate the decrease of the Nusselt number for each fin, when there is a higher intrusion in the cavity.

FIGURE 16

The same investigation performed in Figs. 15 and 16 is repeated for $Ri = 1.0$. Fig. 17a shows the effect of ϕ_1 and ϕ_2 over $\tilde{q}'_{mm}$ and respective optimal shapes and Fig. 17b presents the same effect but considering $\overline{Nu}_{H,mm}$ as performance indicator. Figure 17a shows that asymmetric areas ($\phi_1 = 0.03$ and 0.07) perform better than the cases with symmetric areas ($\phi_1 = \phi_2 = 0.05$), similarly to what previously observed for $Ri = 0.1$. However, for $Ri = 1.0$ the highest magnitude of $\tilde{q}'_{mm}$ is achieved for $\phi_1 = 0.03$ instead of

ϕ_1 = 0.07, which was the best configuration for *Ri* = 0.1. Concerning the optimal ratios, irrespectively of the case analyzed, it was obtained $(H_2/L_2)_o = (H_1/L_1)_{oo} = 10.0$. Comparing the worst with the best case, it was observed an increase of approximately 21% over $\tilde{q}'_{mm}$, showing the importance to examine asymmetrical fins configurations. When $\overline{Nu}_{H,mm}$ is considered as a performance indicator, as in Fig. 17b, results show that asymmetric areas also operate better than the symmetric configuration.

Moreover, the best shapes obtained with ϕ_1 = 0.03 and ϕ_1 = 0.07 led to a similar performance. Concerning the optimal ratios, the best shapes for *Ri* = 1.0 are achieved for more intrusive fins in comparison with those reached for *Ri* = 0.1. This behavior can be related to the restriction of the main vortex in the upper region of the cavity due to the augmented stratification in the convective flow. To increase the interaction between the fins and the main vortex flow, it is necessary to enhance the intrusion of the fins in the cavity.

FIGURE 17

Figure 18 shows the temperature fields related to Figs. 17. As already discussed, the asymmetric cases have shown the best results independently of the Richardson number here investigated (*Ri* = 0.1 or 1.0). It is possible to notice the effect of higher *Ri* in the thermal fields, so that the buoyancy forces become more predominant. For *Ri* = 1.0, the best performance is reached for case 1 (ϕ_1 = 0.03 and ϕ_2 = 0.07) with higher intrusion of the right fin and lower intrusion of left fin. In this configuration, most of the heat is exchanged with the right fin. In addition, case 3 (ϕ_1 = 0.07 and ϕ_2 = 0.03) proved also to reach a good performance. For this condition, the right fin has a lower intrusion in the cavity allowing a higher interaction of the main vortex with the left fin. The temperature fields for $\overline{Nu}_{H,mm}$ are shown in Figs. 18 d – f. The thermal fields morphology clearly illustrates a configuration with higher insertion of the fins in comparison with the scenario obtained for *Ri* = 0.1, induced by the suppression of the main vortex in the upper region of the cavity. It is also noticed that for case 2 ($\phi_1 = \phi_2$=0.05) although the same area distribution occurs for the two fins, the asymmetric configuration appears. This asymmetry was not noticed with reference to the mixed convective flow with *Ri* = 0.1.

FIGURE 18

In general, for both the tested values of *Ri*, it is interesting to note that the results of $\overline{Nu}_{H,mm}$ and $\tilde{q}'_{mm}$ indicate that the best geometric configuration is the asymmetric one. In addition, the best shapes for *Ri* = 0.1 have shown lower ratios, precisely $(H_2/L_2)_o = 0.5$ and $(H_1/L_1)_{oo} = 0.3$, while in the configuration corresponding to *Ri* = 1.0 the fins present a higher intrusion in the cavity, in coherence with the values $(H_2/L_2)_o = 10.0$ and $(H_1/L_1)_{oo} = 3.0$. On the other hand, regarding the evaluation of $\tilde{q}'_{mm}$, there is a trend in which the optimum geometries converge for the ratios $(H_2/L_2)_o = (H_1/L_1)_{oo} = 10.0$. In sum, for different flow regimes (observed in the comparison between *Ri* = 0.1 and 1.0), the effect of the geometric ratios on the thermal performance is also affected, that is, the design depends on the type of flow appearing in the directed cavity. For both $\overline{Nu}_{H,mm}$ and $\tilde{q}'_{mm}$, case 3 is the best one for *Ri* = 0.1, whereas case 1 is the best one for *Ri* = 1.0. Therefore, results showed that the best configuration of the fraction area also depends on the flow regime imposed on the lid-driven flow.

5. CONCLUSIONS

The present work recounts a numerical study on the geometric investigation of two rectangular fins subjected to mixed convective flows in a lid-driven cavity. The flows are considered incompressible, laminar, and in a two-dimensional domain. The study has been carried out using Constructal Design and the optimization procedure is based on the Exhaustive Search method. Two performance indicators have been taken into account, i.e. the dimensionless heat transfer rate per unit length ($\tilde{q}'$) and time and spatial-averaged Nusselt number ($\overline{Nu}_H$). The domain has two degrees of freedom. It was investigated for three different fraction areas (named cases 1, 2, and 3), under two different mixed convective conditions, represented by Richardson numbers of *Ri* = 0.1 and 1.0. For all simulations, the Reynolds and Prandtl numbers were kept constant at the conditions given by $Re_H = 400$ and *Pr* = 6.0.

Results indicated that the choice of the performance indicator plays an important role in the theoretical recommendation about the design of intruded fins in a lid-driven cavity under mixed convective flow. It was demonstrated that the designs that maximize the Nusselt number did not lead necessarily to the highest heat transfer rate, showing that

this parameter depends on the balance between the Nusselt number and heat exchange area of the fins (mainly for the condition imposed here of constant cross sectional areas of the fins). Differences between the best shapes are more significant for flows with Ri = 0.1, i.e. dominated by forced convection. In that cases, the consideration of dimensionless heat transfer rate ($\tilde{q}'$) as performance indicator led to fins with higher intrusion into the driven cavity, while the employment of ($\overline{Nu}_H$) conducted to fins with lower magnitudes for the ratios H_1/L_1 and H_2/L_2. For instance, for Ri = 0.1, the twice maximized dimensionless heat transfer rate ($\tilde{q}'_{mm}$) is obtained for the configurations having ϕ_1 = 0.07, ϕ_2 = 0.03, $(H_2/L_2)_o$ = 10.0 and $(H_1/L_1)_{oo}$ = 10.0, while the twice maximized Nusselt number ($\overline{Nu}_{H,mm}$) is predicted with the configuration, ϕ_1 = 0.07, ϕ_2 = 0.03, $(H_2/L_2)_o$ = 0.5 and $(H_1/L_1)_{oo}$ = 0.3. The augmentation of heat transfer rate is a result of an increase of heat exchange area associated with a slight drop of Nusselt number with the increase of the ratios H_1/L_1 and H_2/L_2. Moreover, results also indicated that the effect of the ratios H_1/L_1 and H_2/L_2 changed significantly for the two investigated performance indicators.

For both the studied Richardson numbers, results indicated that the best geometric configuration was the asymmetric ones, independently of the performance indicator considered. In sum, for different flow regimes (observed in the comparison between Ri = 0.1 and 1.0), the effect of the geometric ratios on the thermal performance is also affected, that is, the design depends on the kind of flow presented in the directed cavity. For both $\overline{Nu}_{H,mm}$ and $\tilde{q}'_{mm}$, scenario 3 is the best one for Ri = 0.1, whereas case 1 is the best one for Ri = 1.0. Therefore, results showed that the best configuration of the fraction area also depends on the flow regime imposed on the lid-driven flow.

All the above remarks highlight the importance of the geometric evaluation for a theoretical recommendation on the geometric configurations that lead to the best thermal performance.

6. ACKNOWLEDGMENTS

P. M. Rodrigues thanks CAPES (Coordination for the Improvement of Higher Educational Personal) for Master Science Scholarship (Finance Code 001). C. C. de Escobar thanks CAPES for financial support in PNPD Program. E.D. dos Santos, L.A. Isoldi, and L.A.O. Rocha thank CNPq (National Counsel of Technological and Scientific Development – Brasília, DF, Brazil) for a research grant (Process: 306024/2017-9,

306012/2017-0 and 307791/2019-0). C. Biserni is sponsored by the Italian Ministry for Education, University and Research.

7. REFERENCES

[1] E.D. dos Santos, G.L. Piccoli, F.H.R. França, A.P. Petry, Analysis of mixed convection in transient laminar and turbulent flows in driven cavities, Int. J. Heat Mass Transf. 54 (21) (2011) 4585-4595.

[2] E. Erturk, C. Gökçöl, Fourth-order compact formulation of Navier–Stokes equations and driven cavity flow at high Reynolds numbers, Int. J. Numer. Meth. Fl. 50 (4) (2006) 421-436.

[3] J.V. Indukuri, R. Maniyeri, Numerical simulation of oscillating lid driven square cavity, Alex. Eng. J. 57(4) (2018) 2609-2625.

[4] R. Iwatsu, J.M. Hyun, K. Kuwahara, Mixed convection in a driven cavity with a stable vertical temperature gradient, Int. J. Heat Mass Transf. 36(6) (1993) 1601-1608.

[5] M. Sheikholeslami, S.A. Shehzad, F.M. Abbasi, Z. Li, Nanofluid flow and forced convection heat transfer due to Lorentz forces in a porous lid driven cubic enclosure with hot obstacle, Comput. Method Appl. M. 338 (2018) 491-505.

[6] A.K. Prasad, J.R. Koseff, Combined forced and natural convection heat transfer in a deep lid-driven cavity flow, Int. J. Heat Fluid Flow 17 (1996) 460-467.

[7] T.S. Cheng, W.H. Liu, Effect of temperature gradient orientation on the characteristics of mixed convection flow in a lid-driven square cavity, Comput. Fluids 39 (6) (2010) 965-978.

[8] K.M. Gangawane, B. Manikandan, Mixed convection characteristics in lid-driven cavity containing heated triangular block, Chinese J. Chem. Eng. 25 (10) (2017) 1381-1394.

[9] T.P. Chiang, W.H. Sheu, R.R. Hwang, Effect of Reynolds number on the eddy structure in a lid-driven cavity, Int. J. Numer. Meth. Fl. 26 (5) (1998) 557-579.

[10] H.N. Dixit, V. Babu, Simulation of high Rayleigh number natural convection in a square cavity using the lattice Boltzmann method, Int. J. Heat Mass Transf. 49 (3) (2006) 727-739.

[11] M.K. Moallemi, K.S. Jang, Prandtl number effects on laminar mixed convection heat transfer in a lid-driven cavity, Int. J. Heat Mass Transf. 35 (8) (1992) 1881-1892.

[12] A.K. Kareem, H.A. Mohammed, A.K. Hussein, S. Gao, Numerical investigation of

mixed convection heat transfer of nanofluids in a lid-driven trapezoidal cavity, International Communications in Heat and Mass Transfer 77 (2016) 195-205.
[13] H.F. Oztop, Z. Zhao, B. Yu, Fluid flow due to combined convection in lid-driven enclosure having a circular body, Int. J. Heat Fluid Flow 30 (5) (2009) 886-901.
[14] K. Khanafer, S.M. Aithal, Mixed convection heat transfer in a lid-driven cavity with a rotating circular cylinder, Int. Commun. Heat Mass Transf. 86 (2017) 131-142.
[15] N.S. Gibanov, M.A. Sheremet, H.F. Oztop, K. Al-Salem, Convective heat transfer in a lid-driven cavity with a heat-conducting solid backward step under the effect of buoyancy force, Int. J. Heat Mass Transf. 112 (2017) 158-168.
[16] K.M. Gangawane, H.F. Oztop, M.E. Ali, Mixed convection in a lid-driven cavity containing triangular block with constant heat flux: Effect of location of block, Int. J. Mech. Sci. 152 (2019) 492-511.
[17] C. Sun, B. Yu, H.F. Oztop, Y. Wang, J. Wei, Control of mixed convection in lid-driven enclosures using conductive triangular fins, Int. J. Heat Mass Transf. 54 (4) (2011) 894-909.
[18] X. Shi, J.M. Khodadadi, Periodic state of fluid flow and heat transfer in a lid-driven cavity due to an oscillating thin fin, Int. J. Heat Mass Transf. 48 (25) (2005) 5323-5337.
[19] M. Hatami, J. Zhou, J. Geng, D. Song, D. Jing, Optimization of a lid-driven T-shaped porous cavity to improve the nanofluids mixed convection heat transfer, J. Mol. Liq. 231 (2017) 620-631.
[20] A. Bejan, Shape and Structure, From Engineering to Nature, Cambridge University Press, New York, 2000.
[21] S. Lorente, A. Bejan, Design With Constructal Law, Wiley, Hoboben, NJ, 2008.
[22] P. Zane, A. Bejan, Design in Nature, Doubleday, New York, 2012.
[23] A. Bejan, S. Lorente, The constructal law and the evolution of design in nature, Phys. Life Rev. 8 (3) (2011) 209-240.
[24] A.H. Reis, A. Bejan, Constructal theory of global circulation and climate, Int. J. Heat Mass Transf. 49 (11) (2006) 1857-1875.
[25] G.W. Merkx, A. Bejan, Constructal Theory of Social Dynamics, Springer, New York, 2007.
[26] L.A. Isoldi, E.D. dos Santos, M.N. Gomes, L.A.O. Rocha, The Constructal Design Applied to Renewable Energy Systems, In: Sustainable Energy Technologies, Eds. E. Rincón-Mejía, A. de las Heras, CRC Press - Taylor & Francis Group, Boca Raton, 2017, pp. 63-87.

[27] G.M. Barros, G. Lorenzini, L.A. Isoldi, L.A.O. Rocha, E.D. dos Santos, Influence of mixed convection laminar flows on the geometrical evaluation of a triangular arrangement of circular cylinders, Int. J. Heat Mass Transf. 114 (2017) 1188-1200.

[28] H. Feng, L. Chen, Z. Xie, Multi-disciplinary, multi-objective and multi-scale constructal optimizations for heat and mass transfer processes performed in Naval University of Engineering, a review, Int. J. Heat Mass Transf. 115 (2017) 86-98.

[29] H. Feng, L. Chen, Z. Xie, F. Sun, Constructal design for gas-turbine blade based on minimization of maximum thermal resistance, Appl. Therm. Eng. 90 (2015) 792-797.

[30] M.R. Hajmohammadi, Introducing a ψ-shaped cavity for cooling a heat generating medium, Int. J. Therm. Sci. 121 (2017) 204-212.

[31] D. Helbig, C.C.C. da Silva, M.V. Real, E.D. dos Santos, L.A. Isoldi, L.A.O. Rocha, Study About Buckling Phenomenon in Perforated Thin Steel Plates Employing Computational Modeling and Constructal Design Method, Latin Am. J. Sol. Struct. 13 (2016) 1912-1936.

[32] M. Mirzaei, H. Hajabdollahi, H. Fadakar, Multi-objective optimization of shell-and-tube heat exchanger by constructal theory, Appl. Therm. Eng. 125 (2017) 9-19.

[33] M. Mosa, M. Labat, S. Lorente, Role of flow architectures on the design of radiant cooling panels, a constructal approach, Appl. Therm. Eng. 150 (2019) 1345-1352.

[34] Z. Xie, L. Chen, F. Sun, Geometry optimization of T-shaped cavities according to constructal theory, Math. Comput. Model. 52(9) (2010) 1538-1546.

[35] E.D. dos Santos, L.A. Isoldi, J.A. Souza, M.M. Goulart, M.K. Rodrigues, F.M. Seibt, R.V. de Souza, L.A.O. Rocha, Constructal design of a rectangular fin intruded into forced convective lid-driven cavity flows, Proceedings Constructal Law Conference 1 (2013) 126–134.

[36] G. Lorenzini, B.S. Machado, L.A. Isoldi, E.D. dos Santos, L.A.O. Rocha, Constructal Design of Rectangular Fin Intruded Into Mixed Convective Lid-Driven Cavity Flows, ASME-J. Heat Transf. 138 (10) (2016) 102501-1 - 102501-12.

[37] E.S. Aldrighi, P.M. Rodrigues, B.D. do A. Rodriguez, L.A. Isoldi, L.A.O. Rocha, E.D. dos Santos, Constructal Design of Rectangular Fin Intruded into Different Surfaces of Forced Convective Lid-Driven Cavity Flow, Int. J. Fluid Mech. Res. 43 (5-6) (2016) 418-440.

[38] A.L. Razera, R.J.C. da Fonseca, L.A. Isoldi, E.D. dos Santos, L.A.O. Rocha, C. Biserni, Constructal design of a semi-elliptical fin inserted in a lid-driven square cavity with mixed convection, Int. J. Heat Mass Transf. 126 (2018) 81-94.

[39] D.D. Gray, A. Giorgini, The validity of the boussinesq approximation for liquids and gases, Int. J. Heat Mass Transf. 19 (5) (1976) 545-551.

[40] A. Bejan, Convection Heat Transfer, John Wiley & Sons, New Tork, 2013.

[41] C. Geuzaine, J.-F. Remacle, Gmsh: A 3-D finite element mesh generator with built-in pre- and post-processing facilities, Int. J. Numer. Meth. Eng. 79 (11) (2009) 1309-1331.

[42] ANSYS. 14.0.—FLUENT User's Guide, ANSYS Inc., 2011.

[43] S. Patankar, Numerical Heat Transfer and Fluid Flow, CRC Press, 1980.

[44] H.K. Versteeg, W. Malalasekera, An Introduction to Computational Fluid Dynamics: The Finite Volume Method, Pearson Education, 2007.

[45] T.H. Ji, S.Y. Kim, J.M. Hyun, Transient mixed convection in an enclosure driven by a sliding lid, Heat Mass Transf. 43 (7) (2007) 629 - 638.

Figures Caption

Figure 1 – Schematic representation of the domain of lid-driven cavity flow with two inserted rectangular fins.

Figure 2 – Flowchart of geometric optimization performed with Constructal Design and Exhaustive Search.

Figure 3 – Instantaneous variables as function of time (t^*) for mixed convective flow with Re_H = 400, Pr = 6.0 and Ri = 0.1 in different cavity placements: a) u^* (Y^* = 0.27); b) T^*(Y^* = 0.27), c) u^*(Y^* = 0.48); d) T^*(Y^* = 0.48), e) u^*(Y^* = 0.93); b) T^* (Y^* = 0.93).

Figure 4 – Effect of the ratio H_1/L_1 over the performance indicators for various ratios of H_2/L_2, Ri = 0.1, ϕ_1 = 0.03 and ϕ_2 = 0.07: a) $\tilde{q}'$, b) $\overline{Nu}_H$.

Figure 5 – Temperature fields obtained from Fig. 4 with the best and worst performance reached for different ratios of H_2/L_2, Ri = 0.1, ϕ_1 = 0.03 and ϕ_2 = 0.07.

Figure 6 – Effect of the H_2/L_2 ratio on the once maximized performance indicators and its optimal shapes, $(H_1/L_1)_o$, for Ri = 0.1, ϕ_1 = 0.03 and ϕ_2 = 0.07: a) $\tilde{q}'_m$, b) $\overline{Nu}_{H,m}$.

Figure 7 – Effect of the ratio H_1/L_1 over the performance indicators for various ratios of H_2/L_2, Ri = 0.1, ϕ_1 = 0.05 and ϕ_2 = 0.05: a) $\tilde{q}'$, b) $\overline{Nu}_H$.

Figure 8 – Effect of the ratio H_2/L_2 on the once maximized performance indicators and its optimal shapes, $(H_1/L_1)_o$, for Ri = 0.1, ϕ_1 = 0.05 and ϕ_2 = 0.05: a) $\tilde{q}'_m$, b) $\overline{Nu}_{H,m}$ Figure 9 – Temperature fields obtained for some once optimized shapes predicted in Fig. 8 for Ri = 0.1, ϕ_1 = 0.05 and ϕ_2 = 0.05.

Figure 10 – Effect of the ratio H_1/L_1 over performance indicators for various ratios of H_2/L_2, Ri = 0.1, ϕ_1 = 0.07 and ϕ_2 = 0.03: a) $\tilde{q}'$, b) $\overline{Nu}_H$.

Figure 11 – Effect of the H_2/L_2 ratio on the once maximized performance indicators and its optimal shapes, $(H_1/L_1)_o$, for Ri = 0.1, ϕ_1 = 0.07 and ϕ_2 = 0.03: a) $\tilde{q}'_m$, b) $\overline{Nu}_{H,m}$.

Figure 12 – Effect of the ratio H_1/L_1 over the performance indicators for various ratios of H_2/L_2, Ri = 1.0, ϕ_1 = 0.05 and ϕ_2 = 0.05: a) $\tilde{q}'$, b) $\overline{Nu}_H$.

Figure 13 – Effect of the H_2/L_2 ratio on the once maximized performance indicators and its optimal shapes, $(H_1/L_1)_o$, for Ri = 1.0, ϕ_1 = 0.05 and ϕ_2 = 0.05: a) $\tilde{q}'_m$, b) $\overline{Nu}_{H,m}$.

Figure 14 – Temperature fields obtained from configurations of Fig. 13 with different ratios of H_2/L_2, Ri = 1.0, ϕ_1 = 0.05 and ϕ_2 = 0.05.

Figure 15 – Effect of the fin fraction area (ϕ_1 or ϕ_2) over the twice maximized performance indicators and the respective optimal shapes, $(H_2/L_2)_o$ and $(H_1/L_1)_{oo}$, for Ri = 0.1: a) $\tilde{q}'_{mm}$, b) $\overline{Nu}_{H,mm}$.

Figure 16 – Temperature fields for the twice optimized shapes presented in Fig. 15 for Ri = 0.1.

Figure 17 – Effect of the fin fraction area (ϕ_1 or ϕ_2) over the twice maximized performance indicators and the respective optimal shapes, $(H_2/L_2)_o$ and $(H_1/L_1)_{oo}$, for Ri = 1.0: a) $\tilde{q}'_m$, b) $\overline{Nu}_{H,m}$.

Figure 18 – Temperature fields for the twice optimized shapes presented in Fig. 15 for Ri = 1.0.

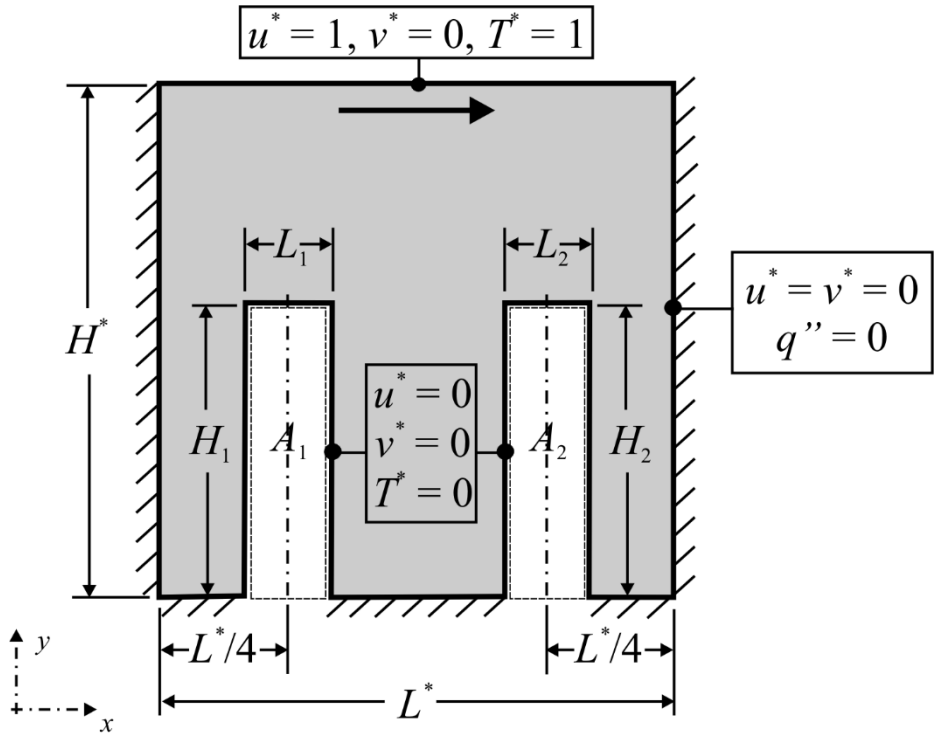

Figure 1 – Schematic representation of the domain of lid-driven cavity flow with two inserted rectangular fins.

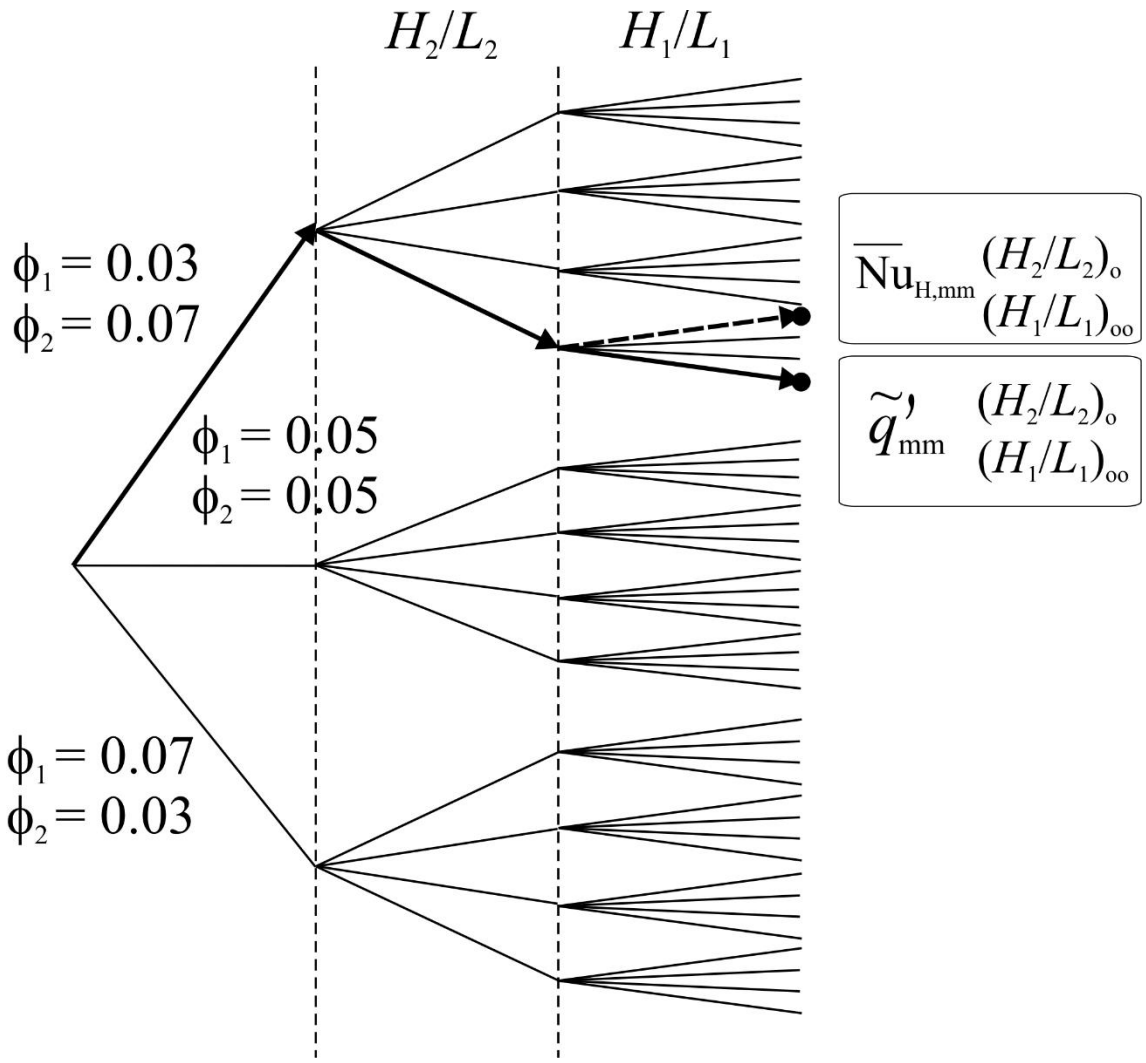

Figure 2 – Flowchart of geometric optimization performed with Constructal Design and Exhaustive Search.

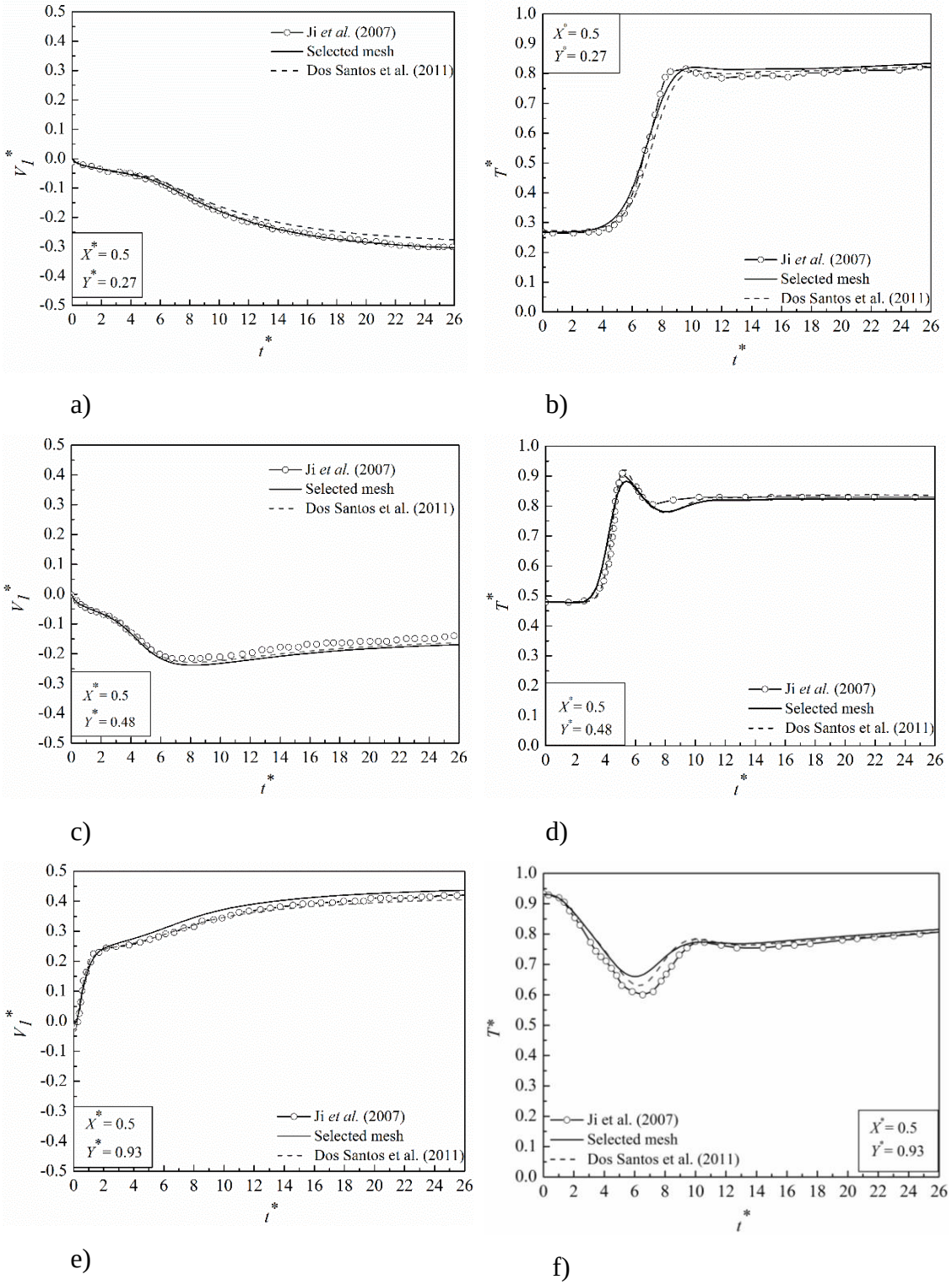

Figure 3 – Instantaneous variables as function of time (t^*) for mixed convective flow with Re_H = 400, Pr = 6.0 and Ri = 0.1 in different cavity placements: a) u^* (Y^* = 0.27); b) T^*(Y^* = 0.27), c) u^*(Y^* = 0.48); d) T^*(Y^* = 0.48), e) u^*(Y^* = 0.93); b) T^* (Y^* = 0.93).

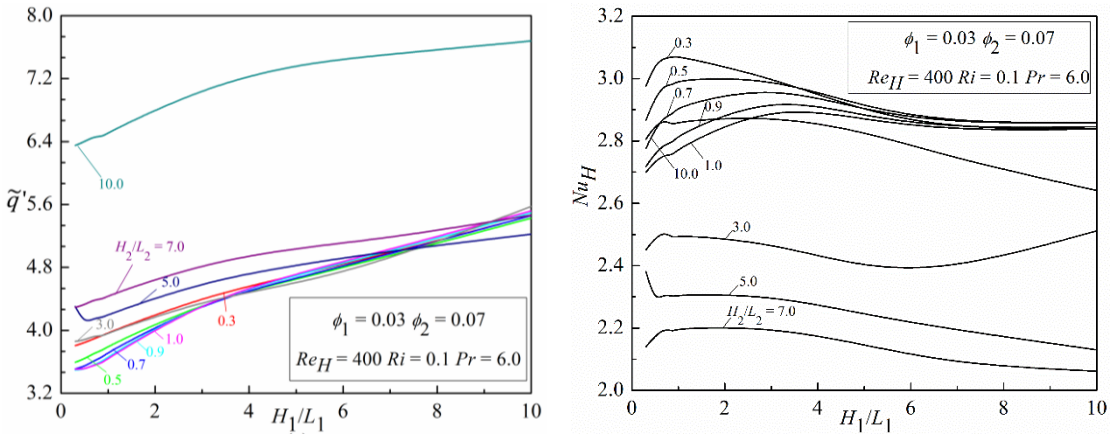

a) b)

Figure 4 – Effect of the ratio H_1/L_1 over the performance indicators for various ratios of H_2/L_2, Ri = 0.1, ϕ_1 = 0.03 and ϕ_2 = 0.07: a) $\tilde{q}'$, b) $\overline{Nu}_H$.

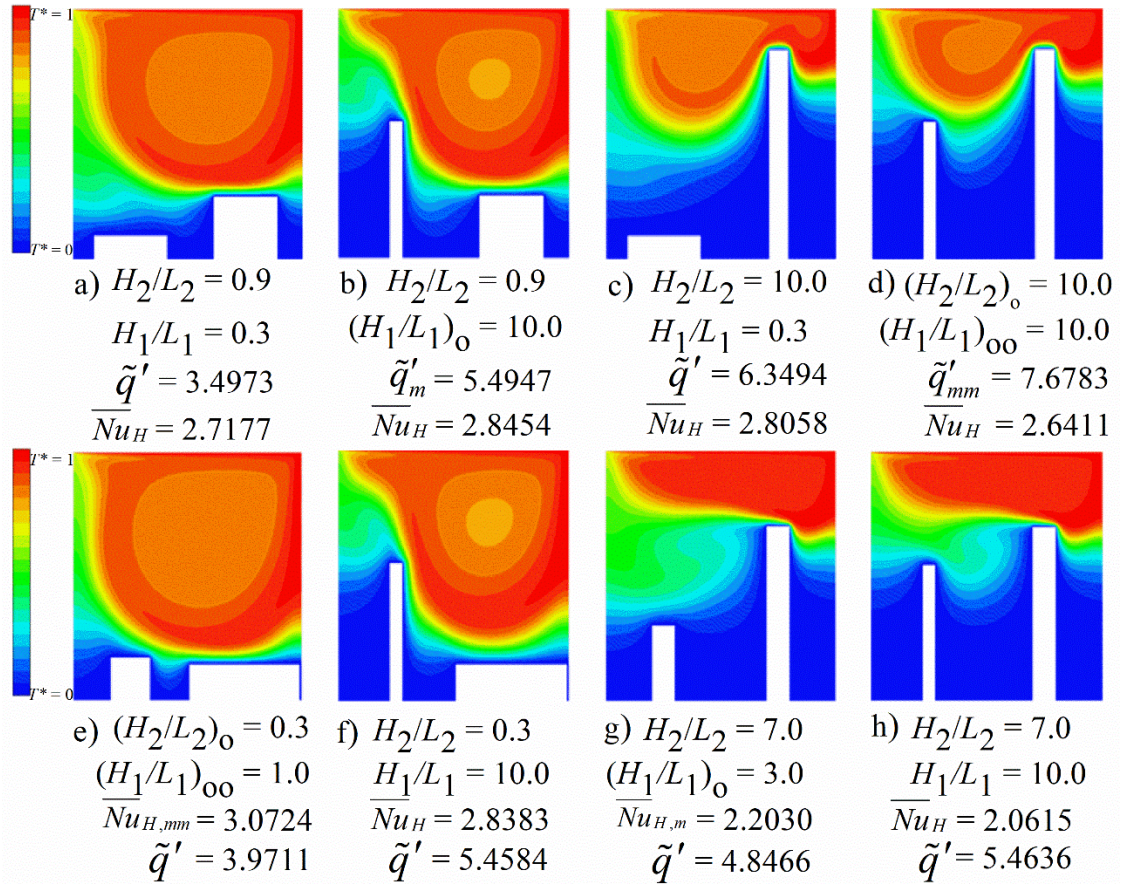

Figure 5 – Temperature fields obtained from Fig. 4 with the best and worst performance reached for different ratios of H_2/L_2, $Ri = 0.1$, $\phi_1 = 0.03$ and $\phi_2 = 0.07$.

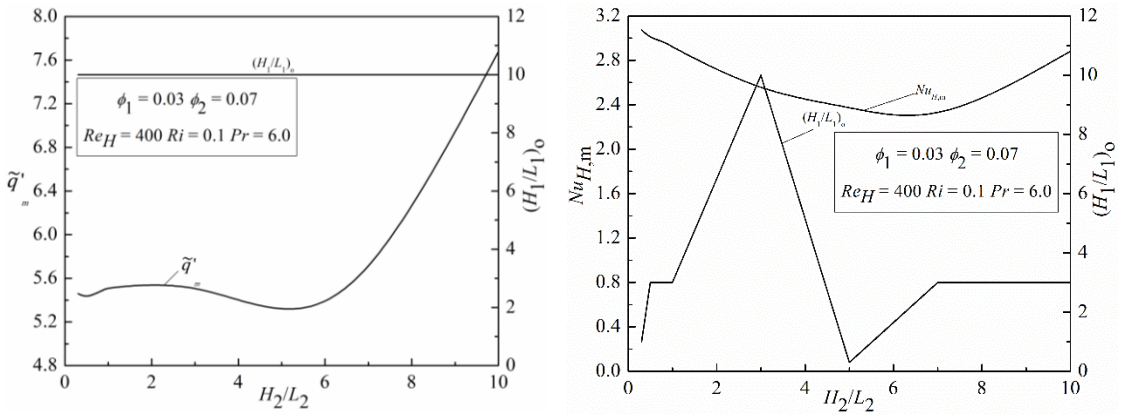

Figure 6 – Effect of the H_2/L_2 ratio on the once maximized performance indicators and its optimal shapes, $(H_1/L_1)_o$, for $Ri = 0.1$, $\phi_1 = 0.03$ and $\phi_2 = 0.07$: a) $\tilde{q}'_m$, b) $\overline{Nu}_{H,m}$.

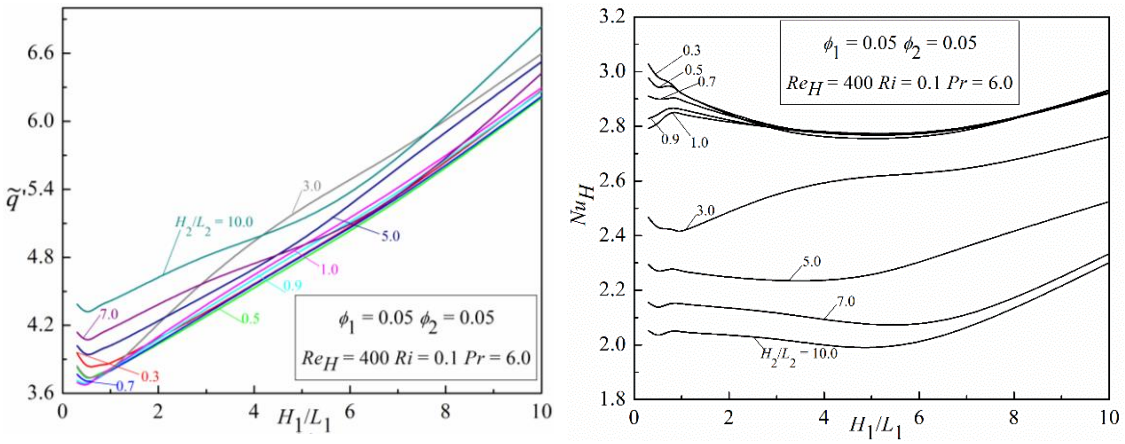

a) b)

Figure 7 – Effect of the ratio H_1/L_1 over the performance indicators for various ratios of H_2/L_2, Ri = 0.1, ϕ_1 = 0.05 and ϕ_2 = 0.05: a) $\tilde{q}'$, b) $\overline{Nu}_H$.

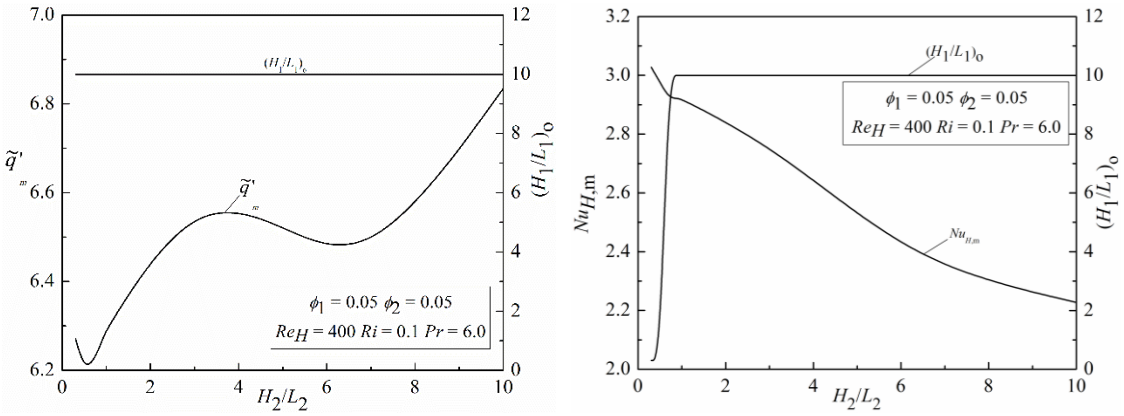

a) b)

Figure 8 – Effect of the ratio H_2/L_2 on the once maximized performance indicators and its optimal shapes, $(H_1/L_1)_o$, for Ri = 0.1, ϕ_1 = 0.05 and ϕ_2 = 0.05: a) $\tilde{q}'_m$, b) $\overline{Nu}_{H,m}$.

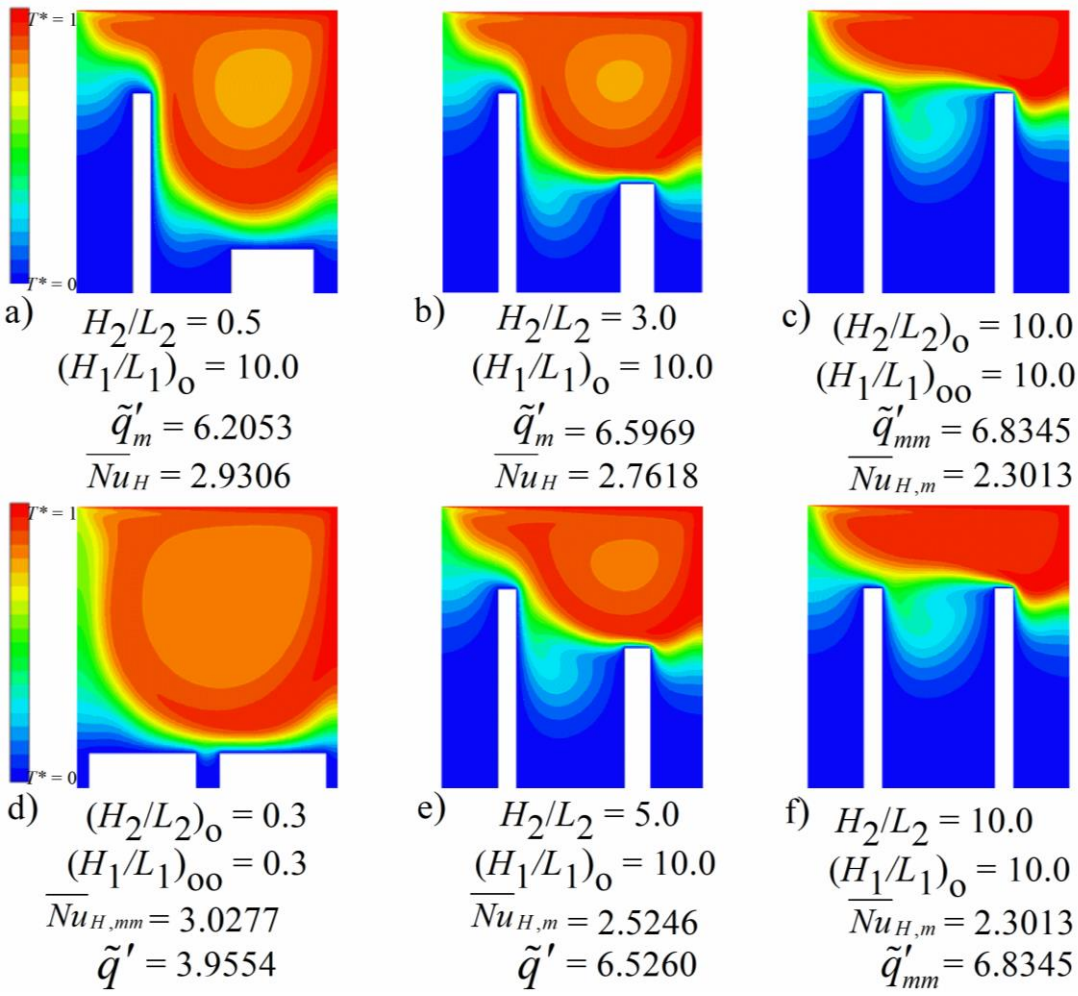

Figure 9 – Temperature fields obtained for some once optimized shapes predicted in Fig. 8 for $Ri = 0.1$, $\phi_1 = 0.05$ and $\phi_2 = 0.05$.

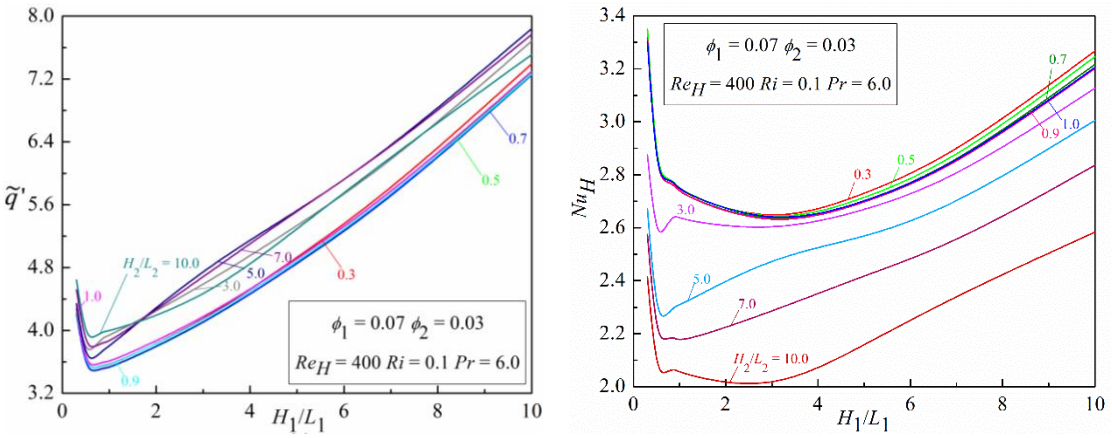

a) b)

Figure 10 – Effect of the ratio H_1/L_1 over performance indicators for various ratios of H_2/L_2, Ri = 0.1, ϕ_1 = 0.07 and ϕ_2 = 0.03: a) $\tilde{q}'$, b) $\overline{Nu}_H$.

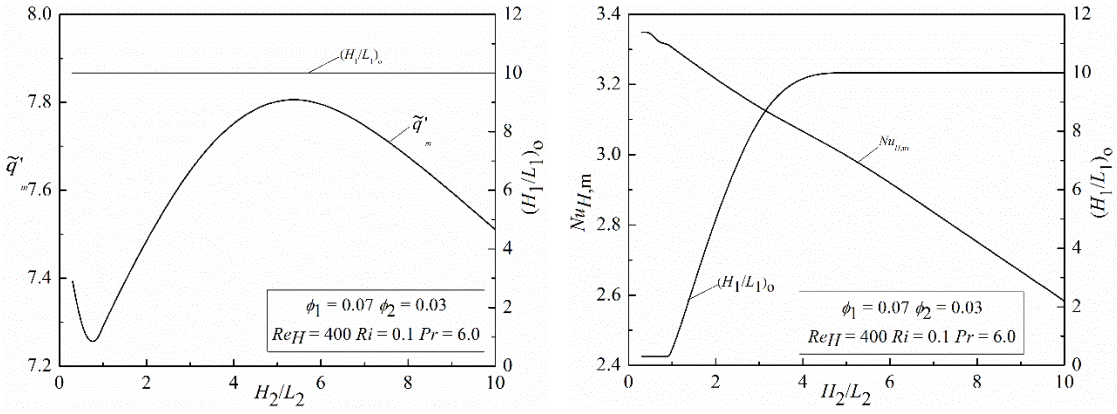

a) b)

Figure 11 – Effect of the H_2/L_2 ratio on the once maximized performance indicators and its optimal shapes, $(H_1/L_1)_o$, for Ri = 0.1, ϕ_1 = 0.07 and ϕ_2 = 0.03: a) $\tilde{q}'_m$, b) $\overline{Nu}_{H,m}$.

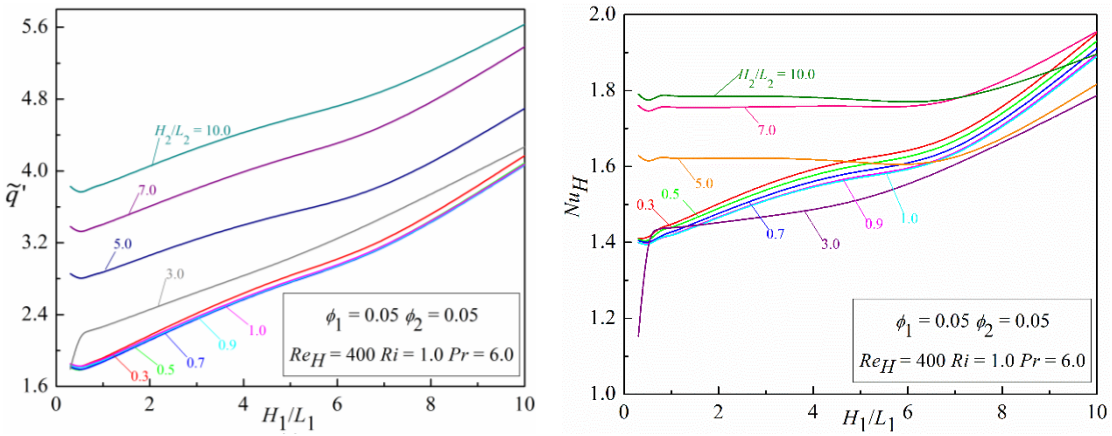

a) b)

Figure 12 – Effect of the ratio H_1/L_1 over the performance indicators for various ratios of H_2/L_2, Ri = 1.0, ϕ_1 = 0.05 and ϕ_2 = 0.05: a) $\tilde{q}'$, b) $\overline{Nu}_H$.

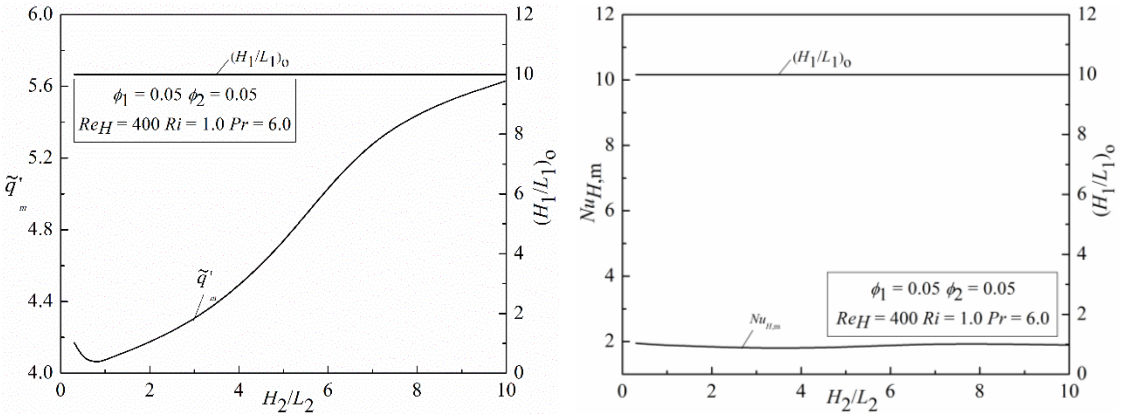

Figure 13 – Effect of the H_2/L_2 ratio on the once maximized performance indicators and its optimal shapes, $(H_1/L_1)_o$, for Ri = 1.0, ϕ_1 = 0.05 and ϕ_2 = 0.05: a) $\tilde{q}'_m$, b) $\overline{Nu}_{H,m}$.

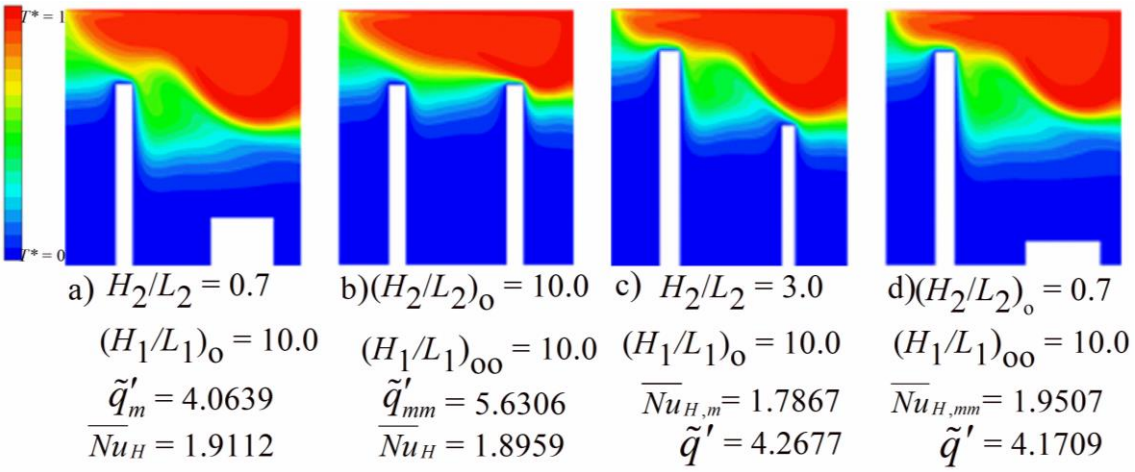

Figure 14 – Temperature fields obtained from configurations of Fig. 13 with different ratios of H_2/L_2, Ri = 1.0, ϕ_1 = 0.05 and ϕ_2 = 0.05.

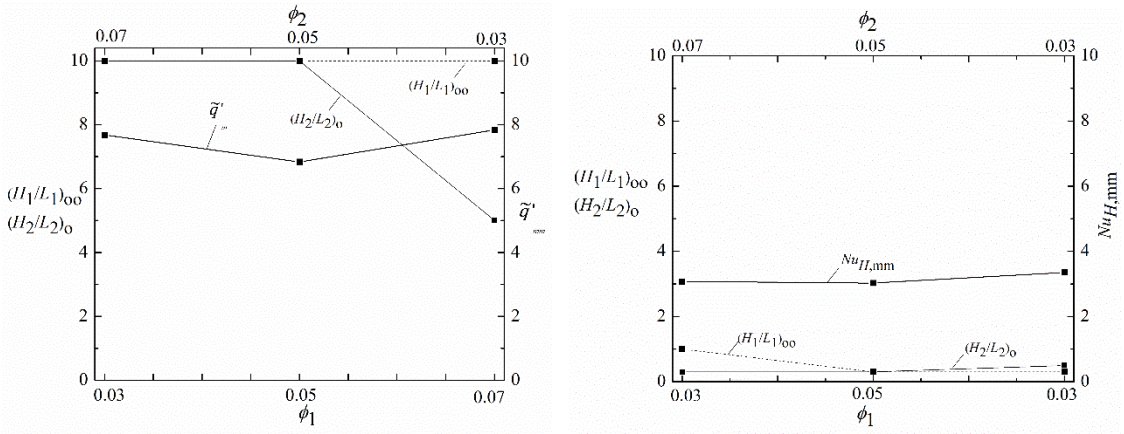

a) b)

Figure 15 – Effect of the fin fraction area (ϕ_1 or ϕ_2) over the twice maximized performance indicators and the respective optimal shapes, $(H_2/L_2)_o$ and $(H_1/L_1)_{oo}$, for Ri = 0.1: a) $\tilde{q}'_{mm}$, b) $\overline{Nu}_{H,mm}$.

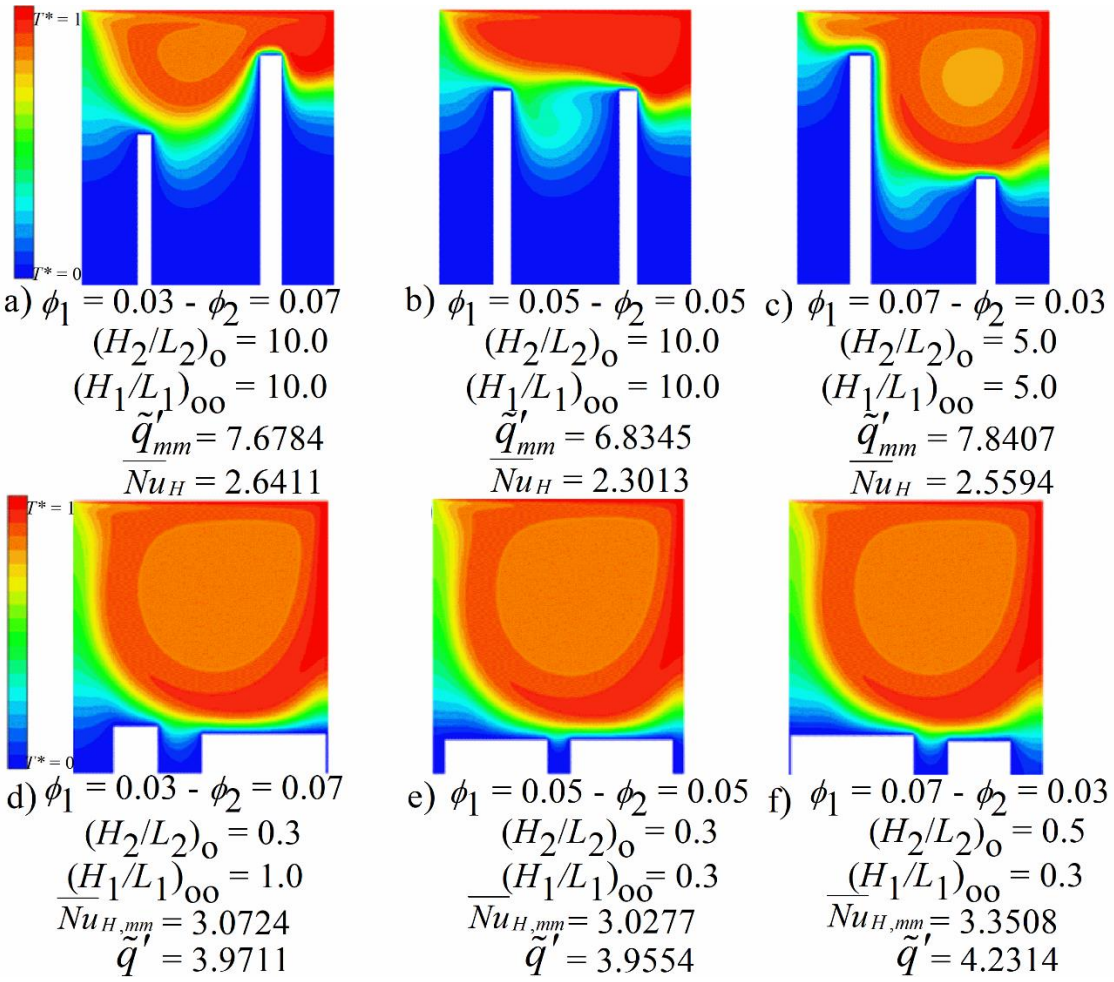

Figure 16 – Temperature fields for the twice optimized shapes presented in Fig. 15 for Ri = 0.1.

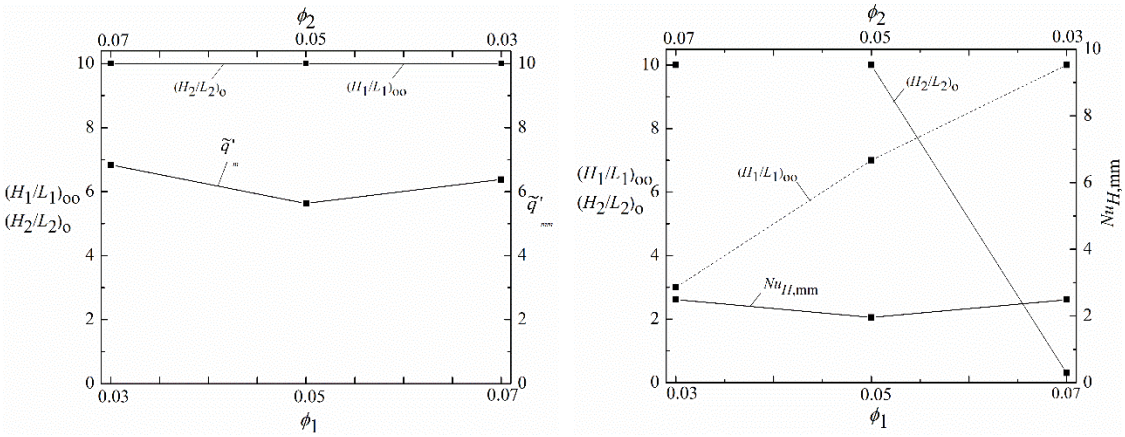

a) b)

Figure 17 – Effect of the fin fraction area (ϕ_1 or ϕ_2) over the twice maximized performance indicators and the respective optimal shapes, $(H_2/L_2)_o$ and $(H_1/L_1)_{oo}$, for Ri = 1.0: a) $\tilde{q}'_{mm}$, b) $\overline{Nu}_{H,mm}$.

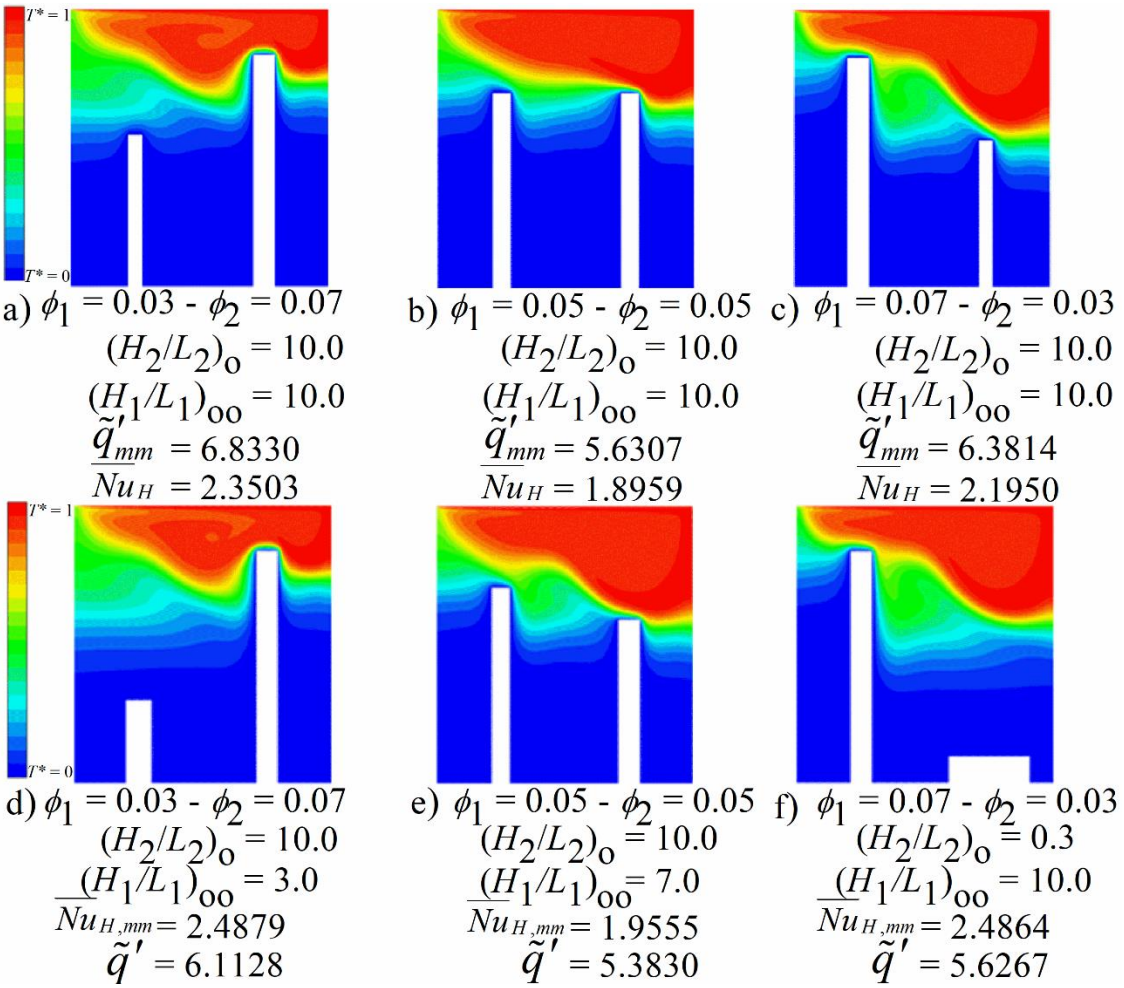

Figure 18 – Temperature fields for the twice optimized shapes presented in Fig. 15 for Ri = 1.0.